ABSTRACT

Title of Thesis: PRESSURE LOSSES IN A NOVEL, VISCOUS SPACECRAFT PROPELLANT AND IMPACTS ON COMPATIBILITY WITH TRADITIONAL MONOPROPELLANT ARCHITECTURES

Timothy Quinn Walsh
Master of Science, 2024

Thesis Directed by: Dr. Christopher Cadou
Department of Aerospace Engineering

Hydrazine offers a unique list of benefits as a spacecraft propellant that have made it the most selected fuel for chemical in-space propulsion, either in its pure form or as one of its derivatives. This is true for both monopropellant and bipropellant applications, as one of pure hydrazine's many benefits is the ability to simultaneously operate in both modes. However, hydrazine is also very hazardous and requires significant logistics to work with on the ground. As a result, there has been an industry-wide search for high-performance replacements that mitigate the hazards and associated logistics. These have been collectively termed 'green propellants'. Two of the most well-known green propellants, ASCENT and LMP-103S, are ionic liquids that propose to completely replace hydrazine. The focus of this thesis is a third green propellant known as Green Hydrazine Propellant Blend (GHPB). GHPB retains hydrazine as a base constituent, but as a hybrid between the conventional and ionic classes of propellants, it is considered less hazardous. Unlike the previous green propellants, GHPB is designed to be used as a 'drop-in' replacement

with existing hydrazine architectures. However, it is much more viscous than hydrazine leading to uncertainties about pressure losses and cavitation.

The objective of this thesis is to relieve some of this uncertainty by measuring pressure loss and flow rate in four common propulsion system components (a latch valve, a filter, and two venturis) over a range of flow rates that are representative of those encountered in an operational spacecraft. The data are used to infer the minor loss coefficient (for non-cavitating flows) and the discharge coefficient (for cavitating flows) as functions of flow rate for each component. Knowing the values of these coefficients is crucial for predicting thruster injection pressures and hence for designing a propellant delivery system. The values of these coefficients as well as the true pressure losses are plotted as functions of flow rate. Pressure losses are found to be approximately 5 times higher than those associated with hydrazine for a given flow rate.

These results are put into context by using them to calculate the pressure distribution in the propulsion system of the Plankton, Aerosol, Cloud, ocean Ecosystem (PACE) spacecraft if hydrazine were replaced with GHPB. The results show that total pressure losses would be 3-14 times greater with GHPB than with hydrazine over the course of the PACE mission. However, GHPB's higher viscosity also reduces the amplitude of pressure transients associated with startup by about a factor of 3. This means that the venturis needed to protect valves from startup transients in hydrazine-based systems are not needed with GHPB. Eliminating the venturis reduces the total pressure losses associated with GHPB to 1.7 – 8.5 times those associated with hydrazine.

PRESSURE LOSSES IN A NOVEL, VISCOUS SPACECRAFT PROPELLANT AND IMPACTS ON COMPATIBILITY WITH TRADITIONAL MONOPROPELLANT ARCHITECTURES

by

Timothy Quinn Walsh

Thesis submitted to the Faculty of the Graduate School of the
University of Maryland, College Park, in partial fulfillment
of the requirements for the degree of
Master of Science
2024

Advisory Committee:
Dr. Christopher Cadou, Chair/Advisor
Dr. Kenneth Yu
Dr. Ray Sedwick
Dr. Eric Cardiff, Special Member

To my parents.

Acknowledgements

There are many people I would like to thank for their support throughout this process. First and foremost, I would like to thank my advisor, Dr. Christopher Cadou, for facilitating a tremendous graduate experience that extended far beyond just this thesis. At your direction, my time at UMD has been meaningful, informative, and challenging. Without a doubt, I am a better engineer for it. I would also like to sincerely thank Dr. Kenneth Yu and Dr. Ray Sedwick for your contributions to this process and my educational experience.

I would like to extend a special thank you to Dr. Eric Cardiff, my manager at NASA GSFC. Your technical leadership was likewise vital to the development of this work, and I am especially grateful for your unwavering support of my educational goals. There were certainly times where my academic obligations conflicted with my professional responsibilities, and it is clear that I would not have been able to accomplish this without such a flexible and supportive manager.

Most importantly, I would like to thank my family for their constant support in all that I do. This is especially true of my parents, who have worked tirelessly my whole life to provide me with the opportunities needed to succeed in everything that I pursue. Your sacrifices, guidance, and steadfast support form the foundation for all that I have achieved, and I consider it my greatest blessing to be your son.

Table of Contents

List of Tables

List of Figures

Nomenclature

Symbols

A	Tube Cross-Sectional Area
A_t	Tube Cross-Sectional Area at the Throat
a	Wave Speed
C_C	Contraction Coefficient
C_d	Discharge Coefficient
C_{d_o}	Discharge Coefficient with respect to Initial Stagnation Conditions
C_dA	Product of Discharge Coefficient and Component Inlet Area
C_E	Expansion Coefficient
cP	Centipoise
D	Tube Diameter
D_t	Tube Diameter at the Throat
f	Darcy Friction Factor
g	Acceleration due to Gravity
h	Height
ID	Inner Diameter
in	inches
I_{sp}	Specific Impulse
K	Minor Loss Coefficient
K_t	Minor Loss Coefficient with respect to the Throat Area
$K_{t_{SC}}$	Minor Loss Coefficient for a Sudden Contraction
$K_{t_{SE}}$	Minor Loss Coefficient for a Sudden Expansion
L	Tube Length
L_{eq}	Equivalent Length
l_e	Entrance Length
$\dot{m}$	Mass Flow Rate
P	Pressure
Q	Volumetric Flow Rate
Q_{ideal}	Ideal Volumetric Flow Rate
R_e	Reynolds Number
SG_{Cl}	Specific Gravity of the Calibrated Liquid
SG_{Tl}	Specific Gravity of the Test Liquid
U_x	Uncertainty in variable x, which is representative of multiple other variables defined here individually
u	Velocity
$\bar{u}$	Average velocity
u_t	Velocity at a Throat
β	Upstream Velocity Parameter
β_t	Upstream Velocity Parameter for Cavitation at a Throat
ΔP	Pressure Differential
ΔP_{loss}	Total Pressure Loss

ΔP_{major}	Major Pressure Loss
ΔP_{minor}	Minor Pressure Loss
Δu	Instantaneous Change in Velocity
ΔV	Change in Spacecraft Velocity
θ_C	Contraction Half-Angle
θ_E	Expansion Half-Angle
μ	Dynamic Viscosity
ν	Kinematic Viscosity
ρ	Density

Abbreviations

A-50	Aerozine-50
AEGL	Acute Exposure Guideline Levels
AN	Army-Navy
BOL	Beginning of Life
COTS	Commercially Available Off-the-Shelf
cSt	Centistokes
CT	Catch Tank
DOT	Department of Transportation
DPG	Differential Pressure Gauge
EOL	End of Life
FDV	Fill & Drain Valve
G1	Pressure Gauge
GHPB	Green Hydrazine Propellant Blend
GHS	Globally Harmonized System of Classification and Labeling of Chemicals
GPM	Gallons per Minute
GSFC	Goddard Space Flight Center
g/ml	Grams per Milliliter
lbm/s	Pound-Mass per Second
MEOP	Maximum Expected Operating Pressure
MMH	Monomethylhydrazine
NASA	National Aeronautics and Space Administration
NIOSH	National Institute of Occupational Safety and Health
OD	Outer Diameter
OSHA	Occupational Safety and Health Administration
PACE	Plankton, Aerosol, Cloud, ocean Ecosystem
PPE	Personal Protective Equipment
PPM	Parts per Million
PSI	Pounds per Square Inch
PSIG	Pounds per Square Inch Gauge
PSID	Pounds per Square Inch Differential
PT	Propellant Tank
R^2	Coefficient of Determination
SCAPE	Self-Contained Atmospheric Protection Ensemble
SI	International System of Units

TWA	Time-Weighted Average
UDMH	Unsymmetrical Dimethylhydrazine
US	United States

Chapter 1: Introduction

1.1 Hydrazine Background

Hydrazine (N_2H_4) is the standard fuel for chemical in-space propulsion. It is used on most spacecraft in either its high purity form, which will hereafter be referred to simply as hydrazine, or as one of its derivatives: monomethylhydrazine (MMH), unsymmetrical dimethylhydrazine (UDMH), or Aerozine-50 (A-50), which is an even mixture of hydrazine and UDMH. It has many beneficial characteristics that make it an ideal choice as a fuel. For example, it is well understood with a large amount of heritage data, it is storable and stable at room temperatures, it provides a high specific impulse (I_{sp}) as either a monopropellant or bipropellant, and its properties are similar enough to water that ground tests can often use water as a substitute [1]. For these and many other reasons, hydrazine has been a stalwart of the space industry for decades despite many drawbacks. Most of the drawbacks stem from its volatile tendencies, especially that it readily decomposes exothermically, which makes it useful as a satellite fuel but hazardous for people who work with it.

The Globally Harmonized System of Classification and Labeling of Chemicals (GHS), which was adopted within the United States via the Occupational Safety and Health Administration's (OSHA) Hazard Communication Standard, will be recognizable to most readers in pictogram form [2]. Hydrazine's GHS pictogram is shown in Figure 1.1, designating it as flammable, acutely toxic, a health hazard, corrosive, and an irritant.

Figure 1.1: Hydrazine's GHS Pictogram [3]

However, a review of hydrazine's safety data sheet shows that the GHS pictogram provides only a surface level description of the associated hazards [3]. For example, hydrazine's flammability designation is more comprehensive than the typical flammability hazard that is familiar to most people, which requires a fuel, oxidizer, and ignition source. This is because hydrazine is hypergolic with oxidizing reagents, meaning they will ignite spontaneously upon contact without an additional energy source. It can also decompose exothermically without the presence of an oxidizer when exposed to an external heat source or material incompatibility, including many metallic oxides. For example, the auto-ignition temperature of hydrazine when exposed to rust is only 74 ºF [4]. This decomposition can also lead to thermal runaway, a circular chain reaction that occurs when decomposition leads to an increase in pressure and temperature, which leads to additional decomposition. This is one of several ways hydrazine can become an explosion hazard in a confined vessel [5].

Furthermore, the threat hydrazine poses to humans does not just present itself as a catalyst for dangerous situations, it is also very dangerous to humans in its unreacted state as well. Specifically, it can cause severe burns with short durations of contact, and it is toxic if inhaled, absorbed, or ingested with consequences up to and including death. It is also a confirmed

carcinogen in animals, is assumed to be for humans, and is known to cause pneumonia, liver and kidney damage, and to target the central nervous system. As a result, acute exposure guideline levels (AEGL) have been determined through collaboration of various international organizations and shown in Table 1.1. In addition to the AEGLs, the National Institute of Occupational Safety and Health (NIOSH) sets an "Immediately Dangerous to Life or Health" value of 50 parts per million (ppm). This is defined as the minimum quantity that is likely to cause death, permeant health effects, or impairment that prevents the person from removing themselves from the dangerous situation [6].

Table 1.1: Hydrazine Health Effect Limits [4]

AEGLs	10 minutes (ppm)	30 minutes (ppm)	60 minutes (ppm)	4 Hours (ppm)	8 Hours (ppm)
AEGL 1: Notable discomfort, irritation, or certain asymptomatic non-sensory effects. However, the effects are not disabling and are transient and reversible upon cessation of exposure	0.1	0.1	0.1	0.1	0.1
AEGL 2: Irreversible or other serious, long-lasting adverse health effects or an impaired ability to escape	23	16	13	3.1	1.6
AEGL 3: Life-threatening health effects or death	64	45	35	8.9	4.4

As shown in the table, relatively low exposures can have drastic consequences on human life. Exactly how much margin is placed between these limits and allowable workplace exposure

limits varies between organizations, but they are all conservative. OSHA enforces a maximum time-weighted average (TWA) of 1 ppm but recommends a value of 0.03 ppm. Other occupational safety organizations enforce even stricter requirements, as shown in Table 1.2. These limits are assuming a standard 40-hour work week and are set to the highest level permissible without risking adverse effects. [7].

Table 1.2: Permissible Hydrazine Exposure Limits by Organization [3]

Organization	TWA (ppm)
OSHA	1.0
ACGIH	0.01
NIOSH	0.03
California DIR	0.01
NASA	0.01

The National Aeronautics and Space Administration (NASA) abides by the most stringent recommendations, and consequently, Hydrazine operations are only conducted with a large amount of planning, oversight, and protective equipment. For laboratory quantities this can sometimes be accomplished with engineering controls, which usually mean that work occurs within a fume hood. However, cases requiring volumes large enough to load a spacecraft require the use of a what is known as a Self-Contained Atmospheric Protection Ensemble (SCAPE). These are positive pressure, totally encapsulating, chemically resistant suits that entirely isolate the person from the propellant they are working with; they are required to either contain their own breathing apparatus or accommodate a pressurized air supply from outside the building that is linked directly into the suit [8]. These suits are certified to strict NASA standards and can cost more than $10,000 each [9].

Figure 1.2: Employees Working in SCAPE [10]

Despite being a well-understood process by now, SCAPE operations come with many challenges. Although the specifics may vary by organization, there is a general industry standard requiring SCAPE operators to undergo a comprehensive certification process, which limits the number of available employees to assist in propellant operations. In addition, operators are limited in their allowable number of SCAPE hours to four per day. The cumulative result of these and many more regulations is a significant additional cost on launch programs in terms of schedule rigidity, additional planning efforts, required training, equipment, limited labor, and more. If there were an efficient alternative to Hydrazine that did not require operations in SCAPE, propellant loading would be faster, cheaper, and much less complex. As a result, the space industry has been searching for a ‘green propellant’ to serve as an alternative to hydrazine in some or all applications.

1.2 History of Green Propellants

"Green Propellant" is an umbrella term without a specific definition, but it is generally understood to mean any propellant with significantly reduced toxicity as compared to conventional propellants, resulting in safer storage and handling [11,12]. While the term propellant can refer to both fuels and oxidizers in either monopropellant or bipropellant applications, green propellant efforts thus far have generally been focused on monopropellant applications. In particular, there have been two well-known green propellants to have undergone advanced research and development, both of which are monopropellants.

AF-M315E, also known by its commercial name "ASCENT", is a hydroxylammonium nitrate-based propellant developed by the Air Force Research Laboratory. It does not include hydrazine or the stringent handling requirements that come with it, and it was successfully demonstrated as a functional propellant on the Green Propellant Infusion Mission [13]. While it offers distinct advantages, namely the simplified ground operations and increased density-I_{sp}, there are significant drawbacks when compared to hydrazine as well. Specifically, ASCENT increases thermal demands on the propulsion subsystem, requires novel or redesigned hardware, and is not able to be cold started. A cold start refers to firing a monopropellant thruster without preheating its catalyst bed. Preheating is standard practice to prevent premature degradation of the catalyst bed, and by extension the thruster, as well as ensuring delivery of the expected thrust. Therefore, although cold starts are avoided whenever possible, it is useful to retain the ability to do so in the event of an unplanned maneuver, launch vehicle tip-off rates that exceed the capabilities of the reaction wheels, or malfunctioning catalyst bed heaters. For that reason, traditional hydrazine

thrusters are normally qualified for a certain number of cold starts with minimal performance losses, and they retain the ability to be cold-started as low as – 20 ºC [14].

An additional green propellant that is well into the maturation process is LMP-103S. This is an ammonium dinitramide-based propellant that was developed by the Swedish company Eurenco Bofors, and it was successfully demonstrated in space on the Swedish-led PRISMA mission [15]. Like ASCENT, it too has a higher density-I_{sp} and drastically relaxed safety requirements, but it also needs increased preheat temperatures, cannot be cold started, and requires redesigned hardware to accommodate elevated decomposition temperatures [16]. While both propellants show promise as a potential replacement and are still under active development, neither has been successful in replacing hydrazine as the industry's primary monopropellant.

ASCENT and LMP-103S are both ionic liquids, which is why they share many of the same advantages and disadvantages when compared to Hydrazine. They are products of a wider industry focus on ionic liquids as a propellant class, which were identified for their low vapor pressure and the corresponding reduction in vapor toxicity [17]. Ionic liquids also tend to be dense, which is another favorable quality for any propellant. However, ionic liquids generally have two major drawbacks by comparison to hydrazine. First, they are not prone to exothermic reactions at the low end of operational temperature ranges, which is why they cannot be cold started. Second, their flame temperatures are beyond the thermal limits of the low-cost nickel-based superalloys that catalyst bed chambers are usually made from. Therefore, there is a design tradeoff with ionic propellants of increased density-I_{sp} and lower toxicity versus increased minimum and operational reaction temperatures [18].

1.3 Green Hydrazine Propellant Blend

Green Hydrazine Propellant Blend (GHPB) is a third green propellant that was created by Aerojet Rocketdyne and selected in the 2020 round of NASA's Announcement of Collaboration Opportunity program to be further developed at Goddard Space Flight Center (GSFC) [19]. The propellant aims to simultaneously maintain the low operational and preheat temperatures of traditional hydrazine as well as the increased density-Isp and low vapor toxicity of the ionic green propellants, effectively making it a hybridization of the two. Consequently, unlike ASCENT and LMP-103S which are hydrazine-free, GHPB still uses hydrazine as a base constituent, but mixed with additives that lower the concentration of hydrazine in the vapor to $1/100^{th}$ of pure hydrazine [18]. This results in a propellant that is safe enough to be used with significantly reduced personal protective equipment (PPE) that still maintains many of hydrazine's advantageous thermal properties. Specifically, GHPB can be cold started, and since it decomposes at temperatures similar to hydrazine, it is compatible with current hydrazine systems without significant redesigns. Together, these qualities address both the developmental and operational constraints of traditional ionic liquids, making GHPB a 'drop-in' replacement for hydrazine. Its drop-in quality has been demonstrated by successful hot fire testing with commercially available hydrazine thrusters, which have also showed I_{sp} to be equivalent to traditional hydrazine. Consequently, the density-I_{sp} of GHPB is approximately 21% greater than hydrazine's (see Table 2.1), which means that when compared to hydrazine, GHPB would provide more ΔV for an identical tank size or an equivalent ΔV while requiring a smaller tank. This can be an important selling point for missions that are expected to be limited in mass margin.

1.3.1: GHPB Hazard Classification

Propellants are subject to range safety requirements set by the governing body at each launch site. These requirements are based on the Department of Transportation's (DOT) assigned hazard classification. For the GPIM mission flying ASCENT, the US Space Force Range Safety classified it as 'critical' as opposed to the 'catastrophic' designation that traditional propellants carry [20]. This is relevant because catastrophic propellants have SCAPE requirements whereas critical propellants do not. Also, a catastrophic propellant requires three electrical and mechanical inhibits to leakage, but a critical propellant only needs two [21]. The corresponding reduction in hardware redundancy results in a cheaper and simpler propulsion subsystem in most cases.

Although GHPB has not yet been rated by the DOT, it has completed parts of the process. It is expected that GHPB will likewise be downgraded to a critical propellant after it receives its full DOT classification, at which point it would likewise be approved for simpler and cheaper range processing than hydrazine.

1.3.2: GHPB PPE

In the same vein, the PPE requirements for operations with GHPB will not be finalized until after the DOT hazard classification process concludes, but the expectation is that large quantity operations will be able to be performed with the same PPE that is currently used for operations with laboratory quantities. For laboratory operations with both GHPB and hydrazine, operators are only required to wear a chemically resistant lab coat, goggles, a face shield, and two sets of nitrile gloves that are each at least 5 mils thick. However, this does assume that other standard safety measures are in place, such as requiring all operations to be done by procedure,

taking steps to secure the facility before hazardous operations begin, and maintaining standard lab safety equipment such as an eyewash station, chemical shower, spill guards, and hydrazine monitors.

Figure 1.3: Engineer Working in GHPB PPE

If these PPE requirements do eventually transfer to operations involving full-scale spacecraft quantities, they will provide flexibility to what is normally an extraordinarily rigid process. This will cut down on planning timelines, increase the personnel that are available for each operation, and simplify loading operations.

1.4 Motivation

Green propellants are not new, as highly concentrated hydrogen peroxide predates hydrazine as a monopropellant and is generally considered green due to its comparatively benign

decomposition products of oxygen and superheated steam. And although specific interest in reducing the toxicity of hydrazine is much more recent, both LMP-103S and ASCENT have existed since the turn of the century, with maturation of technology continuing even after their respective mission demonstrations on PRISMA in 2010 and GPIM in 2019, respectively [22,23]. While interest in green propellant is clearly strong within the United States, the European Space Agency has a unique motivation for investment since there has been consideration of banning hydrazine in the European Union during the last decade, most recently under the Registration, Evaluation, Authorization, and Restriction of Chemicals commission's classification of hydrazine as a "substance of very high concern" [24]. Although no ban has been implemented to date, the specter of a ban has prompted questions about how much longer hydrazine will be readily attainable, and the financial impacts of a ban even if aerospace applications are exempted [25].

Notably, there have been no similar proposals within the United States; however, there is a perennial motivation across the space industry for decreasing budgets, increasing performance, and most especially doing both simultaneously. This is especially true as the industry begins to rely more on smaller satellites, which generally have correspondingly smaller budgets that are less capable of absorbing the considerable fixed cost associated with loading conventional propellants. While there is an assortment of variables that determine the exact cost to load propellant for any specific mission, there is always the potential for significant cost reduction. This was demonstrated in specific detail by the previously referenced PRISMA mission, which operated a traditional hydrazine system in parallel with a system using LMP-103S. A subsequent case study was completed providing a cost comparison between loading operations for the two propulsion subsystems, while also including all contributing costs that are inherent in a loading process. These include managerial and procedural reviews, propellant transport and facility requirements,

training, and waste disposal. The study showed grand totals of $653,099 and $215,144 for the hydrazine and green propellant operations respectively, demonstrating a 67% reduction in cost for this specific mission [26].

Given that the GHPB loading process should retain the same advantages by comparison to hydrazine, it is reasonable to believe that savings for a mission utilizing GHPB would yield similar results. However, there is extra motivation to pursue GHPB when expanding the case study beyond just the loading process. This is illustrated in Table 1.3, which was provided from a separate case study on LMP-103S that was not specific to a particular mission. While categories 2-4 would fall under the loading operations and ancillary costs that were already discussed, category 1 would not. The increased costs in category 1 reflect the need for novel thrusters to accommodate the high-temperature reactions associated with ionic liquid propellants like LMP-103S. This illustrates the primary motivation for pursing GHPB, and its principal distinction from other green propellants: it is a drop-in replacement for hydrazine that operates at similar temperatures and with conventional nickel-based thrusters. This results in hardware costs that are equivalent to hydrazine and significantly below those of the high temperature thrusters required for other green propellants [27].

Table 1.3: Hydrazine vs LMP-103S Cost Comparison adapted from [27]

Categories	Cost Items	Cost Delta (Hydrazine Baseline)
1. Spacecraft Hardware	1N Thrusters	+$20,000/Thruster
	5N Thrusters	+$25,000/Thruster
	22N Thrusters	+$30,000/Thruster
	Propellant Tanks	$0
	Valves, Filters, etc.	$0
2. Propellant & Transportation	Propellant Acquisition	+1,200/Kg
	Propellant Transportation to Site	Launch Site Dependent
3. Launch Processing	Satellite Fueling	-$480,000
	SCAPE Costs	Not Specified
4. Infrastructure	Waste Disposal	-$65/Kg

Notably, SCAPE costs are unspecified in the table, and since GHPB should not require SCAPE, there should be a further cost reduction. Additionally, since GHPB does not use any novel compounds during synthesis, it is not expected to share the significant increase in acquisition price that was reflected in this study for LMP-103S. Put more simply, from a financial perspective, GPHB should enjoy all the benefits of previous green propellants without any of the drawbacks.

1.5 Implications for Industry

Replacing hydrazine without sacrificing performance is not a goal specific to NASA, and although some organizations have invested more heavily in green propellants than others, the entire space industry would benefit from a safe, cost-effective, and high-performance drop-in replacement for hydrazine. As a result, the potential implications for GHPB are enormous. However, it is important to keep a grounded view because hydrazine has a long list of beneficial

qualities that make the bar for replacing it extraordinarily high, and the maturation process for a new propellant is very lengthy.

That being said, within NASA, missions and payloads are assigned a risk classification from A-D with decreasing priority, budget, and risk aversion [28]. It is reasonable to expect that the full extent of GHPB's impact on the industry will be determined by the results of an eventual technology demonstration mission, which hopefully will be the outcome of the work presented here. If GHPB is determined to be a viable propellant with significant advantages compared to hydrazine, a reasonable outcome might be that GHPB is chosen for lower mission classes on a case-by-case basis, but not for missions of the highest priority until the technology is more mature. Likewise, other space organizations maintain their own risk and budget postures and could similarly be interested in GHPB for some or all of their monopropellant missions.

1.6 Objective

Before employing GHPB on a mission, realizing a cost benefit, or impacting the space industry, the propellant must first be qualified for flight. This qualification process is multi-faceted, but one of the key components of the process is to complete what is known as 'flow testing'. Flow testing refers to the process of measuring the pressure drop as a function of flow rate for common propulsion system components. Therefore, the objective of this work is to complete flow testing for GHPB in a mock system, document the findings, and draw conclusions about how this propellant would perform in an actual spacecraft. A full description of flow testing and its objectives is provided in Chapter 2: Flow Test Overview & Theory.

This work also has broader objectives beyond the scope of GHPB. As previously mentioned, ionic liquids offer many benefits that favor their use as a standalone propellant, as with

LMP-103S and ASCENT, or as a component in a hybrid propellant like GHPB. As a result, ionic liquids will likely continue to play an integral role in the field of green propellants. However, ionic liquids are generally very viscous which can cause issues for propellant delivery systems [29]. This is a fundamental motivation for this work. Therefore, one objective of this work is to provide a benchmark performance metric for viscous propellants as a whole. Although the results cannot be used as a direct proxy for any other liquids, given that current data is almost exclusively gathered with water or traditional propellants, these data will be an important reference for any future ionic or hybrid liquids. This is especially true regarding the ultimate conclusions about whether the propellant's viscous nature is disqualifying for use with traditional monopropellant architectures.

1.7 Organization

This thesis is divided into 6 chapters. Chapter 1 introduces green propellants as whole, why they are important, and how GHPB distinguishes itself from previous green propellants. Chapter 2 provides an overview of what flow testing is, the fluid mechanics behind it, and why it is an important milestone in the development of any new propellant. Chapter 3 provides information about preparing for the flow test. This includes prerequisite testing to calibrate components before data acquisition, equipment selection, and a detailed description of how to perform the test itself. Chapter 4 discusses the results of the test by plotting both loss and discharge coefficients as well as true pressure loss as functions of flow rate for each component. Chapter 4 also provides an uncertainty analysis, a brief discussion of material compatibility, and an assessment of process errors. Chapter 5 provides context for the data by predicting how this propellant would have performed on the PACE spacecraft, which is a mission using traditional hydrazine. Specifically,

analytical comparisons are made between the losses for each propellant when subjected to the component layout and operational flow rates on PACE. This mimics what would be a standard process for evaluating the design of a new spacecraft. Lastly, Chapter 6 provides a summary of the work completed, conclusions, and recommendations for future work.

Chapter 2: Flow Test Overview & Theory

The continuity and Bernoulli equations, two of the most famous in fluid mechanics, are shown below as Equations 2.1 and 2.2. Here, $\dot{m}$ represents the mass flow rate, ρ the density, Q the volumetric flow rate, u the fluid velocity, A the cross-sectional flow path area, P the static pressure, g gravity, and h the vertical distance from a defined point of reference. The second term in Bernoulli's equation, $\frac{\rho u^2}{2}$, is known as the dynamic pressure.

$$\dot{m} = \rho u A = \rho Q = \ constant \tag{2.1}$$

$$P + \frac{\rho u^2}{2} + \rho g h = constant \tag{2.2}$$

When taken together, these equations indicate that as a constant-density fluid flows through a restrictive orifice, conservation of mass requires the reduction in flow area to be compensated for by an increase in fluid velocity, which in turn leads to a decrease in static pressure. As the fluid travels out of the orifice back into a flow path area that is equal to the original, the opposite happens, and pressure and velocity return to their original values. However, this is underpinned by several assumptions involved in the underlying principles. For the work presented here, the most relevant is that the flow is assumed to be inviscid so there is no viscous dissipation [30].

In practical applications where fluids are inescapably viscous, the fluid properties will still generally behave as described by these equations, but the static pressure in the downstream section will never fully recover its upstream value due to viscous losses. This is termed the unrecoverable pressure loss, as illustrated in Figure 2.1. In the context of spacecraft propulsion systems,

unrecoverable pressure losses occur as the propellant interacts with the tubing wall or streamlines become disrupted by changes in the flow path [31]. Since the unrecoverable losses are the focus of this test, future mentions of pressure loss are understood to be unrecoverable.

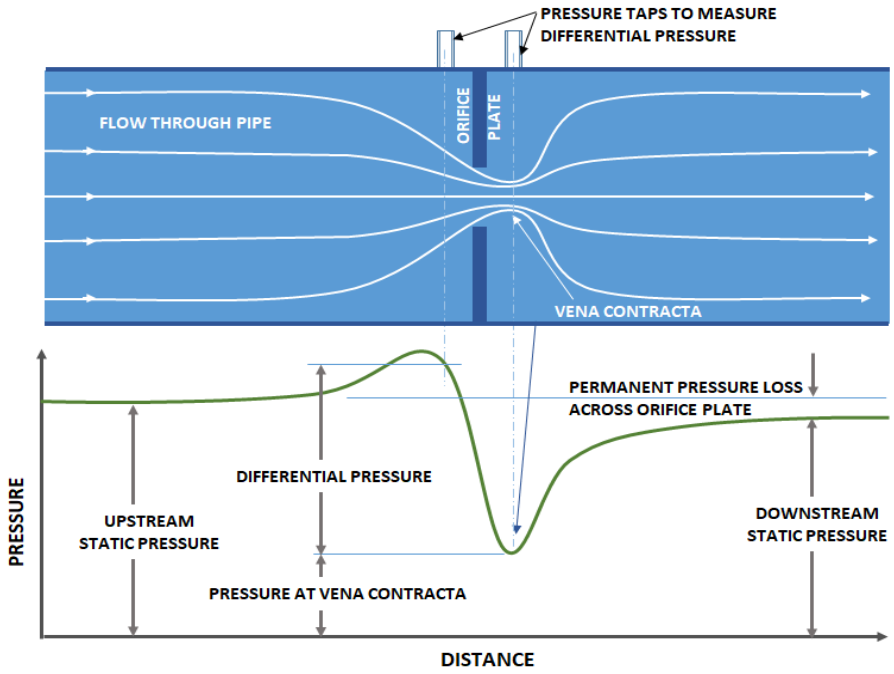

Figure 2.1: Example of Unrecoverable Pressure Loss through an Orifice Plate [32]

Flow testing consists of simultaneously measuring the flow rate and pressure drop across common propulsion system components like valves and filters. It is conducted for two reasons. The first is to determine the upstream pressure, pressure drop, and flow rate at which cavitation will occur in the component. Cavitation sets the component's maximum flow rate, which is used to calculate its discharge coefficient. This is discussed more thoroughly in Chapter 2.2. The second reason is to measure the unrecoverable pressure loss across each component as a function of flow rate, which can be used to determine the component's minor pressure loss coefficient. These are critical metrics for designing a propulsion subsystem for several reasons, but the main reason is that it enables one to determine the thruster injection pressure from the propellant tank pressure. It

is also useful for balancing flows between multiple tanks, which is especially important in bipropellant systems to make sure the propellant mixture ratios remain within the appropriate ranges.

This test is typically conducted with water as a reference liquid due to similarities in material properties between water and traditional propellants. However, the fundamental assumption involved in the water substitution is that the loss coefficient, which is a function of both density and viscosity, is constant between the liquids. Table 2.1 shows that GPHB is approximately 1.21 times denser and 21 times more viscous than traditional hydrazine. This invalidates the water approximation and underscores the need for this test [33]. Note that GHPB's density and viscosity values were measured by GSFC. There are significant disparities in the reported values between GSFC and its industry partners, with the largest disparity being a 44% reduction in viscosity as calculated by Aerojet Rocketdyne [18]. Some disparities are expected because the propellant is manually synthesized in each location, but due to the magnitude of the difference this is still being investigated. The work presented here is based only on the GSFC measured values. Density was measured with an Anton Paar DMA 35N, a U-tube type density meter with an uncertainty of +/- 0.001 g/ml and +/- 0.2 °C. Viscosity was measured with a Cannon 9721-R56 Ubbelohde Viscometer, Size 0B, which has an accuracy of ±0.2%.

Table 2.1: Propellant vs. Water Properties at 20 °C [5,34,35]

Liquid	Density (g/ml)	Dynamic Viscosity (cP)
Water	1	1
GHPB	1.22	21.35
Hydrazine	1.01	0.98
MMH	0.88	0.85

2.1 Unrecoverable Pressure Losses

To predict pressure losses as the propellant flows from the tank to the thruster, the loss across each individual component must first be determined. However, as previously mentioned, these losses are not accounted for in Bernoulli's equation and are difficult to predict analytically. To counter this while still using familiar principles, flows can be analyzed using Equation 2.3 which is sometimes referred to as the modified Bernoulli equation [36].

$$P + \frac{\rho u^2}{2} + \rho gh + \Delta P_{loss} = constant \tag{2.3}$$

Note that this equation is sometimes divided through by ρg, the specific weight of the liquid. In this case, the loss term is referred to as 'head loss' and has units of length. Although this is the preferred method of representing losses in many textbooks, such as in references 30 and 34, this work retains the pressure units since they are more intuitive for spacecraft applications. The choice is arbitrary because Bernoulli's equation is derived from the momentum principle and is fundamentally a statement of conservation of mechanical energy [30]. Consequently, the ΔP_{loss}

term can be regarded as the pressure loss associated with the conversion of mechanical energy to thermal energy through dissipative processes [37]. These mechanical energy losses are broadly classified as 'major' or 'minor' depending on their cause. Therefore, the loss term can be rewritten as shown in Equation 2.4.

$$\Delta P_{loss} = \sum \Delta P_{major} + \sum \Delta P_{minor} \tag{2.4}$$

To visualize this concept, refer to Figure 2.2. The figure provides a simplified schematic for propellant flowing from a tank to a thruster with one valve in the flow path. The major losses are due to friction between the propellant and tubing wall, and the minor loss is induced by the obstruction in the flow path, which in this case is a valve.

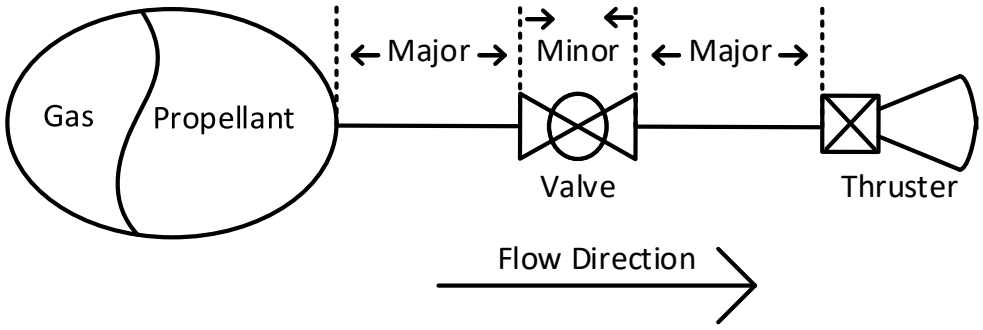

Figure 2.2: Illustration of Major vs Minor Loss

Although a more thorough discussion of major and minor losses is provided in the following 2 sections, there are two oddities to take note of here. The first is that the 'major' and 'minor' loss classification scheme makes sense for oil and gas pipelines (for which it was originally developed), but not for spacecraft propellant systems where components are much closer together and the 'minor' losses dominate. As a result, standard convention within the spacecraft propulsion industry is to refer to major losses as 'line' losses, and minor losses as 'component' losses.

However, in keeping with the literature, the major and minor classifications will be maintained in this work. The second is that although the valve serves as an impediment that induces a large loss, which is classified as a 'minor' loss, there are still frictional effects between the propellant and valve's internal tubing. In that sense, the valve would actually produce both a major and minor loss. However, since the minor loss dominates, the total loss across the valve is simply referred to as the minor loss. This can be mathematically demonstrated by Equation 2.5.

$$\Delta P_{Total_{Valve}} = \Delta P_{Major_{Valve}} + \Delta P_{Minor_{Valve}} \approx \Delta P_{Minor_{Valve}} \tag{2.5}$$

2.1.1 Major Losses

Major losses arise from the shear stress between the fluid and tubing wall when the flow is fully developed, which means the velocity profile is not changing with respect to the x-direction. This occurs at a defined entrance length from the most recent flow path disturbance, for which the exact length depends on the Reynolds number and pipe properties. This is calculated in accordance with Equations 2.6 and 2.7 [30].

$$\text{Laminar Flow: } l_e = 0.06D * Re \tag{2.6}$$

$$\text{Turbulent Flow: } l_e = 4.4D * Re^{\frac{1}{6}} \tag{2.7}$$

However, major losses are excluded from this analysis because they can be determined to within 15% from the flow conditions and pipe properties using Equation 2.8, the Darcy-Weisbach equation [30]. Here, *D* is the diameter of the tube and *L* is the length of tubing that the loss occurs over. Additionally, $\bar{u}$ is the average velocity, which can be calculated from the volumetric flow

rate measurement using Equation 2.1. Lastly, f is the Darcy friction factor. It can be determined from the Colebrook equation, or its better-known graphical form called the Moody diagram [39]. As a result, major losses are sometimes referred to as Moody losses.

$$\Delta P_{major} = f \frac{L}{D} \frac{\rho \bar{u}^2}{2} \tag{2.8}$$

2.1.2 Minor Losses

Minor losses refer to those induced by any changes or impediments in the flow path, such as valve internals, threaded fittings, bends, expansions, contractions, and more. These losses are primarily due to the inertia of the fluid preventing it from following the exact shape of the altered flow path, causing the flow to separate and begin to form swirling patterns known as secondary flows. An example of a secondary flow associated with a 90-degree turn is illustrated in Figure 2.3. Viscous losses associated with separation and reverse flow can be very significant [30].

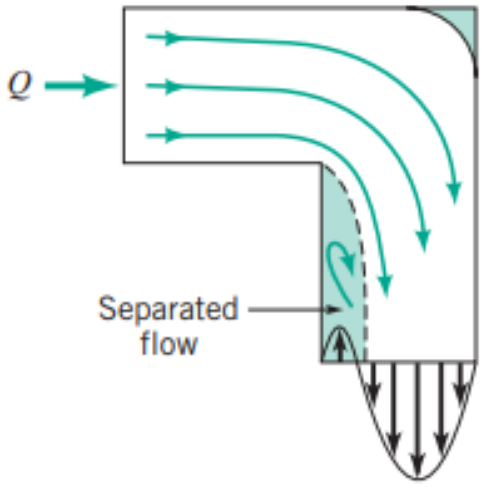

Figure 2.3: Secondary Flow Illustration [36]

Separation bubbles also serve as obstructions that reduce the 'effective' flow path area. For an orifice, this occurs immediately after the throat and is known as the vena contracta. This is where the static pressure of the fluid is at a minimum and the kinetic energy is the highest – a relationship that becomes important during onset of cavitation as discussed in Section

With both major and minor losses now defined, Equation 2.4 can be rewritten in more specific terms. For algebraic simplicity, the minor loss is once again scaled in terms of dynamic pressure as it was in Equation 2.11. Consequently, Equation 2.8 and Equation 2.11 are together inserted into equation 2.4 to solve for the loss term. This is shown as equation 2.22, where *Ki* is being used to indicate a specific K for each component in the flow path. This does assume all components and tubing are in series, that *L* represents the total length of tubing between the tank and thruster, and that *f* and *D* are constant in all tubing.

$$\Delta P_{loss} = \frac{\rho u^2}{2}\left(\frac{fL}{D} + \sum K_i\right) \tag{2.22}$$

This represents the loss that is being used to modify Bernoulli's equation to determine a thruster inlet pressure. The general form is shown as Equation 2.23. *PInlet* represents the thruster inlet pressure, *PTank* represents the tank pressure, and *ΔPloss* is what's solved for in Equation 2.22.

$$P_{Inlet} = P_{Tank} - \Delta P_{loss} \tag{2.23}$$

2.2 . Figure 2.4 provides a more complete view of the flow through an orifice by illustrating the major losses due to the pressure gradient, the unrecoverable loss through an orifice, induced secondary flows, and the vena contracta.

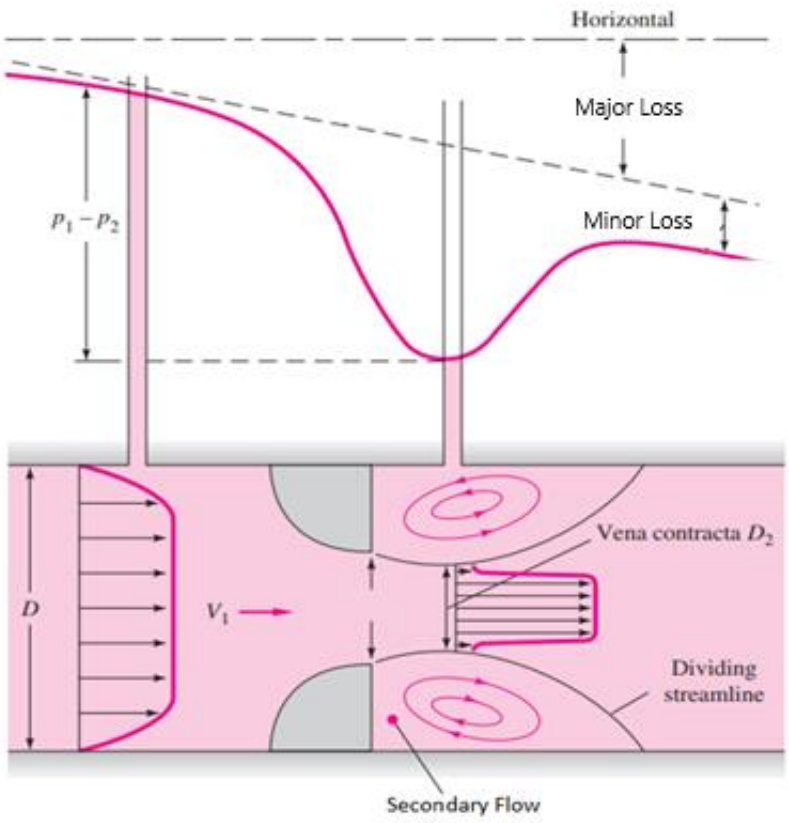

Figure 2.4: Complete Pressure Loss through an Orifice, adapted from [39]

Unlike major losses, minor losses are almost exclusively determined empirically. One way they are measured is by defining an equivalent length (L_{eq}) of straight tube that would produce a major loss equal to the minor loss. This relationship is shown as Equation 2.9 [30].

$$\Delta P_{minor} = f \frac{L_{eq}}{D} \frac{\rho \bar{u}^2}{2} \tag{2.9}$$

Note that in both Equation 2.8 and Equation 2.9, the product of the friction factor and length to diameter ratio is functioning as a multiple of the dynamic pressure. Since dynamic pressure in a tube is generated at the expense of static pressure, the losses in static pressure are typically expressed as a multiple of the dynamic pressure [31].

Given that major losses are calculated analytically while minor losses need to be determined empirically, and that this work is therefore only focused only the latter, we will dispense with the distinction and henceforth simply refer to minor losses as pressure losses. The objective of the two sections that follow is to develop methods for relating measurements of pressures upstream and downstream of a propellant system component to losses occurring within the component. Different approaches are required depending on whether the flow is cavitating.

2.2 Modeling pressure losses when the flow is incompressible.

Our analysis of the incompressible situation begins with Bernoulli's equation in the form of Equation 2.3, written for a streamline passing through a variable area duct as illustrated in Figure 2.5. Body forces are neglected in this analysis.

$$P_1 + \frac{\rho u_1^2}{2} = P_2 + \frac{\rho u_2^2}{2} + \Delta P_{loss} \tag{2.10}$$

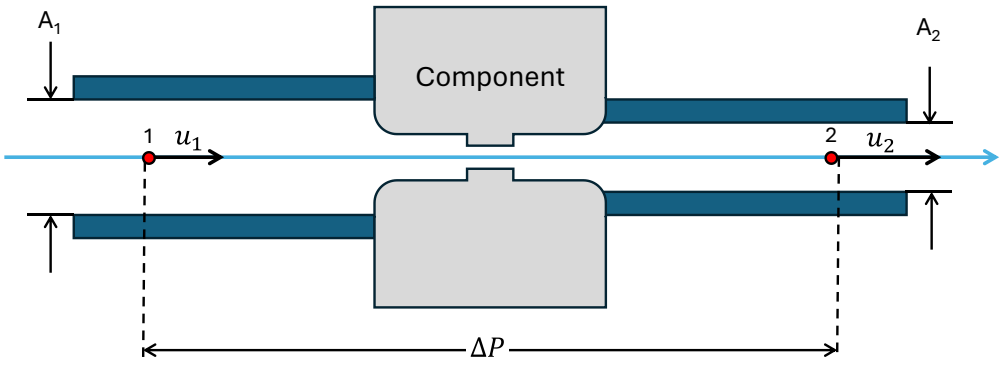

Figure 2.5 Schematic illustration of flow through an arbitrary component

The difference in pressure between stations 1 and 2 in Figure 2.5 is due to the difference in velocity at each station and the unrecoverable pressure loss (ΔP_{loss}). Although the

unrecoverable loss could be represented using the equivalent length method described in the previous section, it is more common to represent the unrecoverable pressure loss using a loss coefficient (*K*) that is defined as follows:

$$K \equiv \frac{\Delta P_{loss}}{\frac{1}{2}\rho u_2^2} \tag{2.11}$$

Note that this equation can be rearranged to once again define the loss in terms of a multiple (which in this case is *K*) of the dynamic pressure. Specifically, the losses are scaled by the dynamic pressure *downstream* of the component (ie. at station 2) to account for situations where the upstream condition is a plenum, and the dynamic pressure is approximately zero. Conservation of mass relates u_1 to u_2:

$$\rho u_1 A_1 = \rho u_2 A_2 \tag{2.12}$$

Inserting Equation 2.11 and 2.12 into 2.10 and rearranging gives:

$$P_1 - P_2 = \frac{\rho u_2^2}{2}\left[1 - \left(\frac{A_2}{A_1}\right)^2 + K\right] \tag{2.13}$$

Inserting the definition of the volume flow rate, $Q = uA$, into Equation 2.12 gives:

$$Q_1 = Q_2 = Q \tag{2.14}$$

The volume flow rate is the same at all points in the flow system because the density is constant. Therefore,

$$u_2 = \frac{Q}{A_2} \tag{2.15}$$

Inserting Equation 2.15 into Equation 2.13 and replacing $P_1 - P_2$ with ΔP gives:

$$\Delta P = \frac{\rho Q^2}{2A_2^2}\left[1 - \left(\frac{A_2}{A_1}\right)^2 + K\right] \tag{2.16}$$

Defining a parameter β such that:

$$\beta = 1 - \left(\frac{A_2}{A_1}\right)^2 \tag{2.17}$$

gives the final expression for the pressure difference between the measurement points, the flow area downstream, and the unrecoverable loss represented as a dimensionless loss coefficient *K*:

$$\Delta P = \frac{\rho Q^2}{2A_2^2}[\beta + K] \tag{2.18}$$

The loss coefficient is what we seek to determine for each flow component. Two limiting cases of Equation 2.18 are important. When the upstream pressure is measured in a large volume like a propellant tank, $A_1 \gg A_2$ and $\beta = 1$. When the upstream pressure is measured at a location with the same flow area as the downstream pressure measurement, $A_1 = A_2$ and $\beta = 0$. In this latter situation, the velocities at stations 1 and 2 are equal so the difference in pressure between stations 1 and 2 is due only to the unrecoverable pressure loss, ie. $\Delta P = \Delta P_{loss}$. This is illustrated in Figure 2.6.

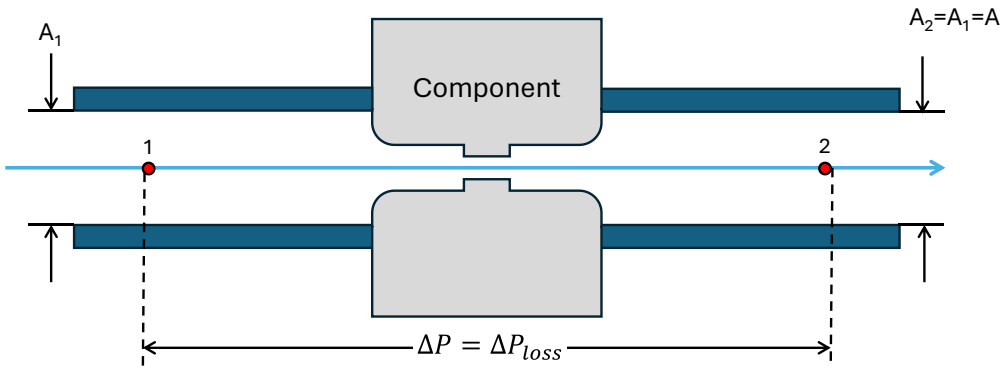

Figure 2.6: Flow through an arbitrary component with equal upstream and downstream areas

In this situation, the pressure difference is due only to the unrecoverable losses between stations 1 and 2. This is the configuration used in the experiments reported here. Solving Equation 2.16 for the loss coefficient with $\beta = 0$ gives the equation used to determine the loss coefficient from the measurements in this work.

$$K = \frac{2}{\rho}\left(\frac{\pi D^2}{4}\right)^2 \frac{\Delta P}{Q^2} \tag{2.19}$$

In this expression, K is the loss coefficient, Q is the measured volumetric flow rate, ΔP is the measured pressure difference across the component, and D is the inner diameter of the tubes leading to and from the component.

Note that in Equation 2.19 the reference area must be input based on the system configuration. Valves and filters used on spacecraft often have complicated or unknown internal geometries, which could make it difficult to define a throat area. Consequently, it is common to use the inlet line inner diameter to determine the reference area for these components. The only exception is for components called 'cavitating venturis', which will hereafter be referred to simply as 'venturis'. A more thorough discussion of venturis is included in Section 2.2, but they are

circular orifices, and their defining characteristic is their throat size. Therefore, the venturi throat area is intrinsically known, and as a result, loss coefficients for venturis are often calculated with respect to their throat area. To indicate that a loss coefficient is calculated with respect the venturi throat area, K_t is used in place of the K. Nonetheless, venturi loss coefficients can just as easily be calculated with respect to the inlet tube area. This is due to the conservation of mass, meaning K and K_t can be related by equating Equation 2.19 to itself.

$$\Delta P = \frac{K\rho}{2}\left(\frac{4Q}{\pi D^2}\right)^2 = \frac{K_t\rho}{2}\left(\frac{4Q}{\pi D_t^2}\right)^2 \tag{2.20}$$

For a given flow rate, this is further reduced to Equation 2.21 [31].

$$K = K_t\left(\frac{D}{D_t}\right)^4 \tag{2.21}$$

With both major and minor losses now defined, Equation 2.4 can be rewritten in more specific terms. For algebraic simplicity, the minor loss is once again scaled in terms of dynamic pressure as it was in Equation 2.11. Consequently, Equation 2.8 and Equation 2.11 are together inserted into equation 2.4 to solve for the loss term. This is shown as equation 2.22, where K_i is being used to indicate a specific K for each component in the flow path. This does assume all components and tubing are in series, that L represents the total length of tubing between the tank and thruster, and that f and D are constant in all tubing.

$$\Delta P_{loss} = \frac{\rho u^2}{2}\left(\frac{fL}{D} + \sum K_i\right) \tag{2.22}$$

This represents the loss that is being used to modify Bernoulli's equation to determine a thruster inlet pressure. The general form is shown as Equation 2.23. P_{Inlet} represents the thruster inlet pressure, P_{Tank} represents the tank pressure, and ΔP_{loss} is what's solved for in Equation 2.22.

$$P_{Inlet} = P_{Tank} - \Delta P_{loss} \tag{2.23}$$

2.2 Modeling pressure losses when the flow is cavitating

Cavitation refers to a phenomenon where the static pressure of a flowing fluid drops below the fluid's vapor pressure. When this happens, some of the fluid comes out of the liquid phase to form vapor cavities/bubbles. While these cavities collapse when the pressure recovers, the density of the flow is no longer constant, which means that an alternative to Bernoulli's equation is needed to model the pressure loss. This section presents such an alternative.

Cavitation occurs in many flows which are not relevant to spacecraft propulsion, like at the tips of a marine propeller (Figure 2.7) or flow over rough surfaces. However, it can also be produced in pipe systems by flow path curvatures, turbulence, reductions in flow area through an orifice, or a combination of these factors [30,37]. When the induced vapor bubbles migrate back into an area of higher pressure and collapse, the corresponding vibrations may cause structural damage over time.

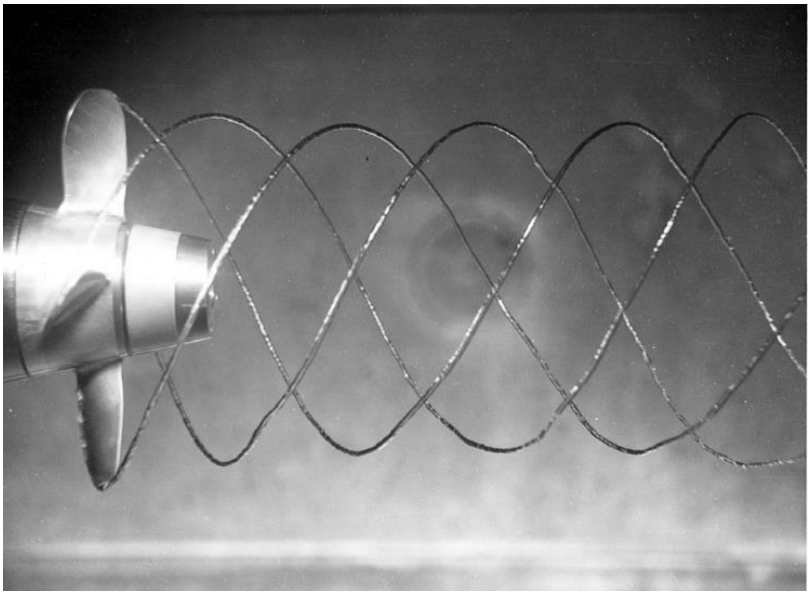

Figure 2.7: Cavitation bubbles mark tip vortices in high-velocity regions of a propeller's wake [40]

However, cavitation is not always undesirable, and it is often induced intentionally on spacecraft as 'bulk' cavitation. 'Bulk' cavitation refers to the case where the pressure falls below the vapor pressure throughout the flow, as opposed to at localized regions associated with bends, turbulence, or surface roughness. As it pertains to spacecraft propellant feed systems, bulk cavitation generally occurs in the converging flow field associated with an orifice. This is illustrated in Figure 2.8, where due to pressure recovery, the pressure difference between the inlet and throat is much larger than the pressure difference (loss) across the orifice. As a result, even components with small overall pressure drops can induce cavitation [37]. When this occurs, the upstream flow becomes decoupled from any further changes in the downstream flow and the flow rate reaches its maximum [30]. For this reason, bulk cavitation is often referred to as 'choked' flow. Although not governed by the same principles as the compressible form of choked flow that often results from sonic conditions at a throat, from a functional standpoint, it can be thought of as the incompressible analog to choked flow because it represents the point where further reductions in downstream pressure will not increase the mass flow rate. At that point, the only way to increase

mass flow rate would be to increase the upstream pressure or flow area, but neither is usually feasible once on orbit.

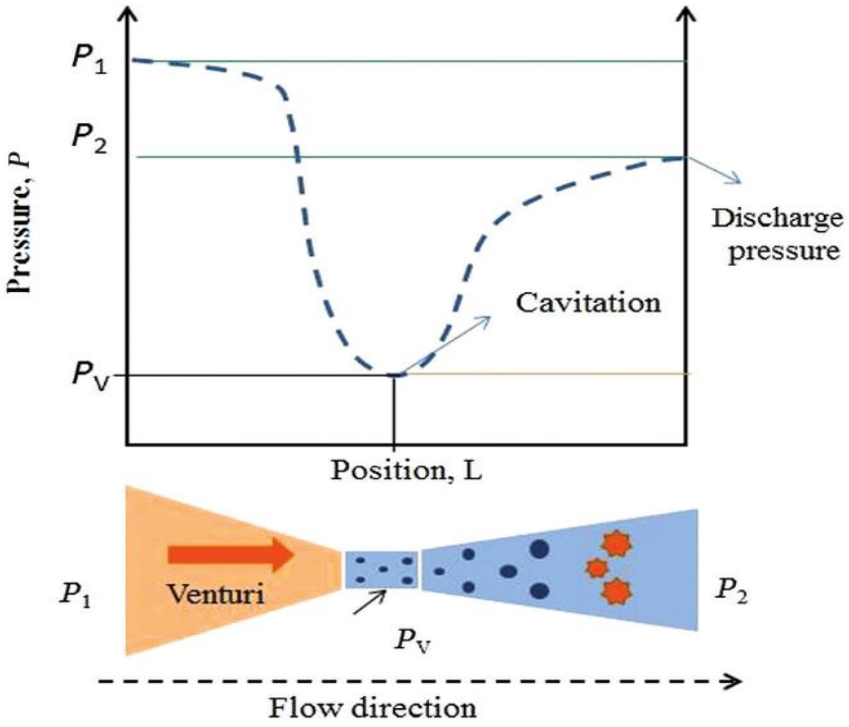

Figure 2.8: Cavitation in an Orifice [41]

This flow limiting property is often exploited to design a maximum flow rate for a given propulsion subsystem, which is necessary to safely initialize the system once on orbit. This is because to comply with range safety requirements regarding three seals for leak prevention, propellant is usually not filled up to the thruster on the launch pad. Instead, there is typically an isolation valve and an empty manifold separating the propellant and thrusters during launch. When the isolation valve is opened on orbit, high-pressure propellant rushing into the empty manifold impacts the dead-end at the thruster valve and can result in hydraulic shock. To combat this, a tapered orifice is usually installed in the manifold to induce cavitation. This limits the maximum flow rate, and by extension the pressure spike associated with this event [33]. These orifices are called venturis, and a (non-spacecraft) example is shown in Figure 2.9.

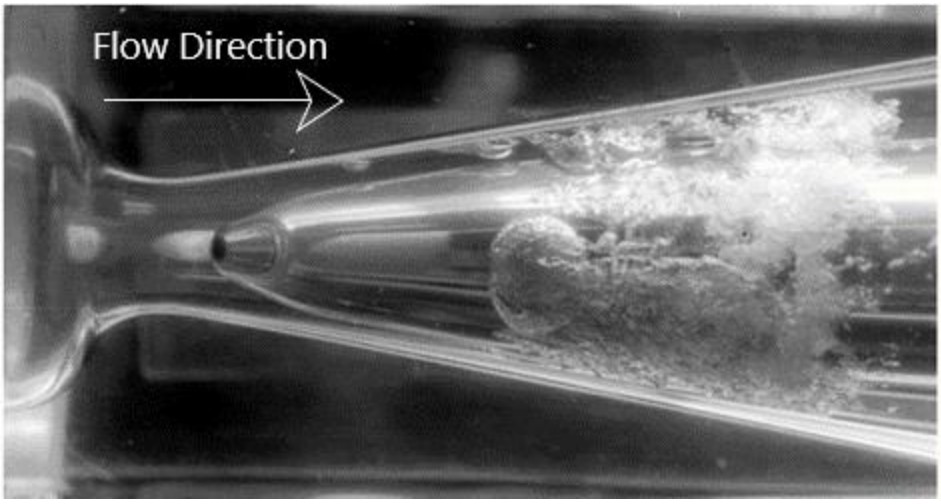

Figure 2.9: Flow Limiting Cavitation in Water-Filled Venturi Tube, adapted from [41]

One of the benefits of intentionally inducing cavitation at a venturi is that it can prevent it from occurring anywhere else. As a result, cavitation for spacecraft applications has a more limited scope than other industries. Specifically, bulk cavitation is the dominant form, and except where otherwise specified, future references to cavitation are intended to mean bulk cavitation with choked flow in a throat. Additionally, since surge flow rates occur only briefly during the aforementioned startup process, noise and long-term damage due to vibrations from collapsing bubbles are not considered relevant issues.

Equation 2.16 can be rearranged with $A_2 = A_t$, $P_2 = P_t$, and $K = 0$ (assuming ideal, inviscid flow) to show that the flow rate through an orifice *prior to cavitation* is proportional to the square root of the pressure drop:

$$Q = \sqrt{\frac{2A_t^2 \Delta P}{\rho\left[1 - \left(\frac{A_t}{A_1}\right)^2\right]}} \tag{2.24}$$

While Equation 2.24 is an idealization, it works very well for flows through venturis until cavitation begins. Beyond the cavitation point, the flow rate remains constant (and at its maximum) as the pressure difference across the orifice continues to increase.

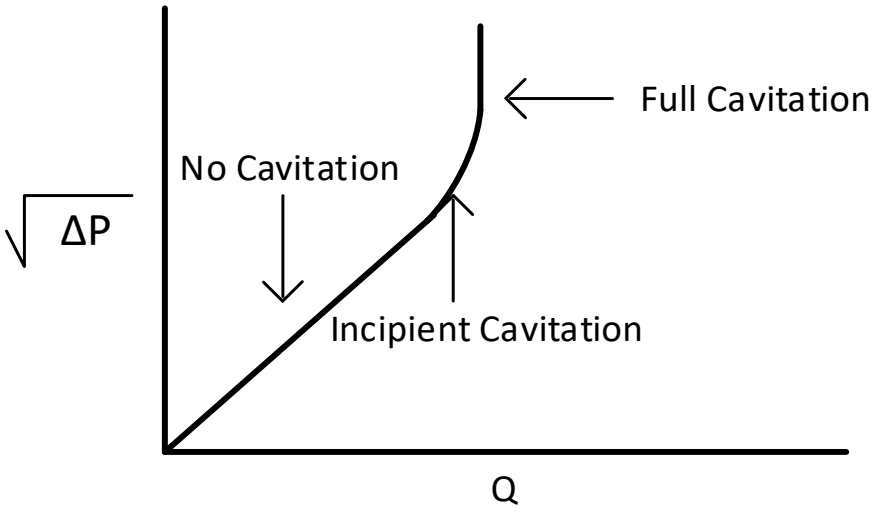

Figure 2.10: Generalized Cavitating Flow Example

The onset of cavitation can be determined by plotting pressure drop as a function of flow rate and observing when the flow rate reaches an asymptote, as illustrated in Figure 2.10. Note that this drawing is not to scale, and the incipient cavitation section is exaggerated for emphasis. Many non-spacecraft applications draw a distinction between incipient and full cavitation due to the differences in the resulting noises and vibrations. These considerations are less important in spacecraft applications so the distinction between incipient and full cavitation is not usually made.

Propulsion systems are typically designed for cavitation to be localized at the throat of a venturi. In order to ensure this, the venturi must have a smaller cavitation flow rate than the rest of the components, thereby inducing cavitation at the venturi before any other components. As previously mentioned, reductions in flow path area are not the only source of cavitation. Complicated geometries or impediments in a component's internal flow path can produce

cavitation in the component before it would occur in a venturi with the same throat size. Since venturis are simple components, they can be used as a point of a reference for other components to determine an 'effective' throat size as a percentage of the actual throat size. Therefore, the effective throat size of a non-venturi component is equal to the venturi throat size that would induce the same cavitation flow rate that the component is inducing. To prevent unexpected cavitation at locations other than the venturi, the designer must ensure the venturi throat is smaller than the *effective* throat sizes of the other components, not their *actual* throat sizes.

Since a cavitating flow is decoupled from the downstream pressure, by extension it is decoupled from the pressure loss across the component as well. As a result, pressure losses in a cavitating flow can no longer be modeled using K, since K is related to the pressure drop. When cavitation occurs, the component is more appropriately modeled as an orifice with a discharge coefficient (C_d). The discharge coefficient is a dimensionless factor used to measure the deviation of the actual flow rate from the ideal (ie. inviscid) flow rate. Therefore, it is defined as the ratio of the actual volumetric flow rate (Q) to the ideal volumetric flow rate (Q_{ideal}).

$$C_d = \frac{Q}{Q_{ideal}} \tag{2.25}$$

Q_{ideal} is determined from the unmodified Bernoulli equation while also ignoring the potential energy term since elevation and gravitational effects are negligible in space. Note that since this is a measure of flow through an orifice, station 2 is now defined at the throat.

$$P_1 + \frac{\rho u_1^2}{2} = P_t + \frac{\rho u_t^2}{2} \tag{2.26}$$

This is re-written algebraically to solve for u_t, which is then related to flow rate using the constant-density form of the continuity equation.

$$u_t = \sqrt{\frac{2(P_1 - P_t)}{\rho} + u_1^2} = \frac{Q_{ideal}}{A_t} \tag{2.27}$$

These relations are substituted back into Equation 2.25 to solve for C_d. The u_1 term can be related to Q in the same manner that u_t was, and noting that $Q_1 = Q_2$ due to mass conservation of a constant density fluid, the equation yields the following form [36]:

$$C_d = \frac{Q\sqrt{\rho\left(1 - \left(\frac{D_t}{D_1}\right)^4\right)}}{A_t\sqrt{2\Delta P}} = \frac{Q}{A_t}\sqrt{\frac{\rho\beta_t}{2\Delta P}} \tag{2.28}$$

where

$$\beta_t = \left[1 - \left(\frac{D_t}{D_1}\right)^4\right] \tag{2.29}$$

Note that the discharge coefficient can be derived with respect to different initial conditions. In Equation 2.28, the upstream conditions are taken to be the inlet of the component, and the downstream conditions are the throat. However, it is also common to derive C_d with respect to initial stagnation conditions (meaning $u_1 = 0$, $P_1 = P_{o_1}$, and thus $\beta_t = 1$) in which case Equation 2.28 reduces to Equation 2.30. These will be differentiated by an additional naught subscript that assumes initial stagnation conditions.

$$C_{d_o} = \frac{Q}{A_t}\sqrt{\frac{\rho}{2\Delta P}} \tag{2.30}$$

Removing the diameter ratio is convenient for the latch valve and filter since unlike venturis, these types of components may have complicated or unknown internal flow-path areas. For this reason, discharge coefficients in this work are calculated with Equation 2.28 for the

venturis, but Equation 2.30 for the latch valve and filter. Note that in a properly designed system flow through the latch valve and filter would not be cavitating, so C_d is generally only calculated for venturis anyway. Regardless, the diameter ratios (D_t/D_1) for the 0.045 in and 0.06 in venturis are 0.14 and 0.19 respectively, meaning that β_t has a negligible effect in Equation 2.28.

Since C_d is independent of the pressure loss across a component once cavitation begins, ΔP in this equation represents the difference between the upstream pressure and the propellant vapor pressure. The propellant vapor pressure is less than 0.5 psia though, meaning ΔP is essentially equal to the driving pressure.

Chapter 3: Test Setup

3.1 Facilities & Propellant Synthesis

All testing and related operations were conducted in a fume hood at NASA GSFC's Area 400 Propulsion Complex. This included propellant synthesis, because GHPB has not yet finished its DOT hazard assessment. As a result, it cannot be shipped on public roads, so all propellant constituents were shipped to GSFC individually and mixed on the premises. The mixing process is straightforward and can be completed quickly for laboratory quantities.

3.2 Methodology

The system was designed in a closed-loop fashion so that it could be refilled without unnecessary exposure to propellant. As a result, a significant amount of the test manifold was used for ancillary operations such as purging or propellant recirculation. For ease of viewing, these elements have been removed from Figure 3.1, which shows the portion of the schematic that functioned as the data acquisition section.

As discussed in Section 2.1, Equations 2.6 and 2.7 provide a method for calculating entrance lengths for the flow to become fully developed based on the Reynolds number and *L/D* ratio of the tube. This method is the preferred method in literature [30,36]. However, in applications where this level of conservatism is not feasible or required, an alternative approach is to use ten times the *L/D* ratio, regardless of Reynolds number, allowing for shorter entrance lengths than those that would be calculated in Equations 2.6 and 2.7 [38]. Due to the need to assemble this system within a fume hood with limited space, this was the approach taken for this work. Although

the minimum *L/D* is 10, straight line lengths of 6 in were achieved at each data acquisition location, which for a diameter of 0.319 in leads to an *L/D* of 19. This was acceptable because the component and tubing connections were made with fittings and adapters. Therefore, although the intention was to induce fully developed flow at the data acquisition points, the inclusion of these fittings and adapters meant that the fully developed flow would be disrupted to some degree at the component inlets regardless. Hand valves and tubing were connected with a combination of Swagelok and 37° flare Army-Navy (AN) fittings, while the remaining components used national pipe thread. All tubing had a wall thickness of 0.028 in and an OD of 3/8 in, except for the fill and drain valve which used 1/4 in OD tubing. The tubing, fittings, and adapters were all a mixture of various grades of stainless steel and titanium.

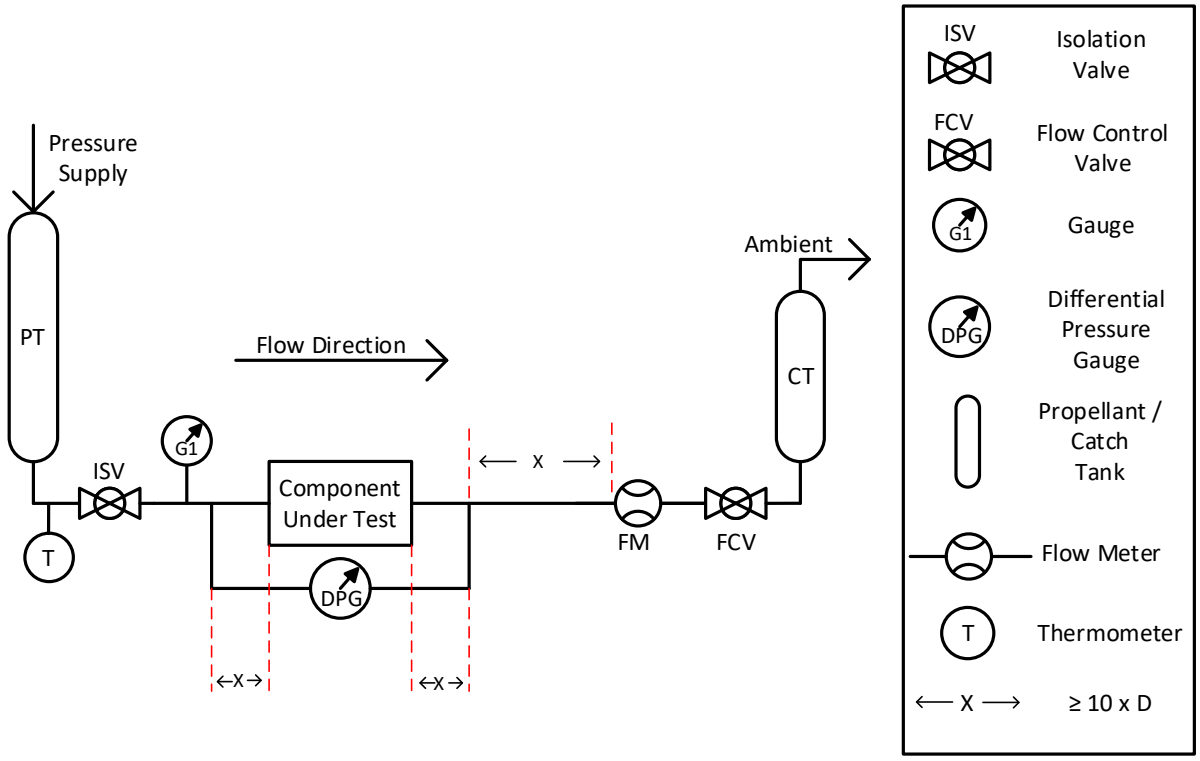

Figure 3.1: Data Acquisition Section of the Flow Testing Schematic

The propellant tank (PT) was pressurized with helium to force propellant across the component under test, which was in parallel with a differential pressure gauge (DPG) and in series with a flow meter and throttle valve (FCV). Propellant exited the flow path into a catch tank (CT) that was open to ambient. Driving pressure was measured at the gauge (G1) upstream of the component under test, which measured gauge pressure. The entire section between the tanks was assembled horizontally to eliminate gravitational effects, which are usually inconsequential on orbit. The completed set-up is shown in Figure 3.2, which is the hardware implementation of the schematic in Figure 3.1. For more information about each data acquisition instrument, refer to Table 3.1: Data Acquisition Hardware.

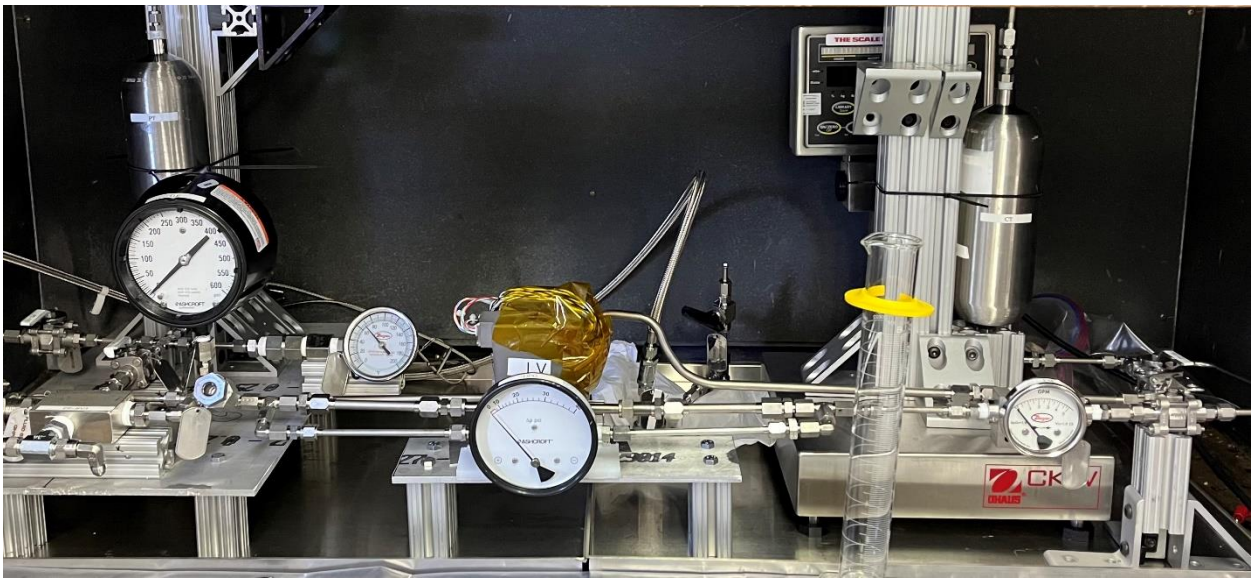

Figure 3.2: Flow Test Apparatus

This testing was performed at driving pressures ranging from 50 – 300 psig. Note that there were no vacuums present for this test, so all subsequent mentions of psi are measures of gauge pressure; atmospheric pressure was not measured, but since the testing occurred in Greenbelt, MD, it can be approximated as 14.7 psia. 50 psi was chosen as the lower bound to approximate what a

standard minimum thruster inlet pressure might be, and the upper bound was limited by component maximum pressure ratings. Flow rates were gradually increased using the throttle valve (FCV) to the maximum achievable value at each driving pressure to determine if and when a component cavitated. In real time, cavitation was indicated by the flow meter reaching a maximum value while the differential pressure reading continued to grow. Nonetheless, the primary range of interest was 0 – 0.95 GPM, or 0-0.16 lbm/s, which represents realistic operational flow rates for monopropellant missions.

3.3 Data Acquisition Hardware

Due to the novelty of the propellant and the explosion hazards associated with its constituents, safety engineering prohibited the use of powered instruments during testing. This restriction will only remain in place until the propellant receives a hazard rating by the DOT and is not expected to be an issue for an actual mission; however, it did preclude the use high-accuracy electrical pressure transducers and flow meters that would normally be standard for this test. As a result, data were not acquired at a constant sample rate as might typically be expected. Rather, the analog gauges were videoed, and data were gathered by reading the gauges manually at different frames. All measuring devices were commercially available off the shelf (COTS) parts, as seen in Table 3.1.

Table 3.1: Data Acquisition Hardware

Hardware	Manufacturer	Part Number	Instrument Type	Accuracy
Pressure Gauge	Ashcroft	45-1279SS-02L-0/600	Bourdon Tube	± 3 psi
Differential Pressure Gauge 1	Ashcroft	45-1130SD-25S-150	Piston	± 3 psi
Differential Pressure Gauge 2	Ashcroft	45-1130SD-25S-40	Piston	± 0.8 psi
Flow Meter	Dwyer	DTFW-1S-5W	Rotameter	± 0.1 GPM
Thermometer	Dwyer	BTB34010D	Bimetal	± 2 °F

Given that testing was for multiple components and each at various flow rates, there was a wide range of differential pressures expected. This meant that two DPGs with different ranges were required to ensure operations were in optimal measurement ranges for the instrument. DPG_1 had a range of 0-150 psid with an accuracy of ±2% of the full scale, but this was only valid for differential pressures greater than or equal to 20 psid; below 20 psid, accuracy was as low as ±5% of the full scale. On the other hand, DPG_2 had a full-scale range 0-40 psid, so this was used for low pressure-differential flows such as line tares and the fill and drain valve. Due to limited space in the fume hood, the gauges were swapped as needed rather than being installed in parallel.

Since the two most relevant variables to this test were density and viscosity, a thermometer was inserted into the flow system to verify temperature; however, all testing was at room temperature and thermometer readings never exceeded the range of 67 °F – 68 °F. As a result, temperature effects were not considered in this work. Although changes in propellant temperature were not able to be induced while adhering to the safety requirements prohibiting power during testing, since viscosity varies temperature, the effect of changes in temperature on the pressure losses will need to be understood across a mission's operational temperature ranges. Propellant feed lines are usually thermostatically controlled within a fairly large range; for example, NASA's

Microwave Anisotropy Probe was designed to accommodate hydrazine temperature variations between 10 °C – 55 °C during nominal operations, and 5 °C – 60 °C during anomalous conditions [43]. The corresponding viscosity ranges are 1.14 cP – 0.62 cP for the nominal case and 1.34 cP – 0.58 cP for the anomalous case, which would have a measurable effect on pressure losses. [5]. Since the unpowered instrumentation requirement is temporary, this presents a key area of future work with

GHPB. 3.4 Flight Components

The flight components that were tested are shown in Table 3.2, and are represented in Figure 3.1 by the white box labeled “component under test”. All of them are former flight spares that are still considered to be representative of standard hardware. The part number for the 0.045 in venturi was not available.

Table 3.2: Flight Components Tested

Component	Manufacturer	Part Number	Line OD (in)
Latch Valve	Vacco	V1E10948-01	0.375
Filter	Vacco	F1D10397-04	0.375
0.06 in Venturi	Fox Valve	621747	0.375
0.045 in Venturi	Fox Valve	-	0.375
Fill & Drain Valve	Moog	50-875	0.25

3.4.1 Latch Valve

Latching solenoid valves, also known as latch valves (see Figure 3.3 for an example), are a type of solenoid valve that can be maintained in either the open or closed state without continuous power. They require an electric pulse (usually on the order of milliseconds in duration) to change

states [44]. They can be used to isolate both liquids and gasses and are very common in propulsion systems due to their effectiveness and power efficiency [45].

Figure 3.3: Example of a Latch Valve [44]

3.4.2 Venturis

As introduced in Chapter

With both major and minor losses now defined, Equation 2.4 can be rewritten in more specific terms. For algebraic simplicity, the minor loss is once again scaled in terms of dynamic pressure as it was in Equation 2.11. Consequently, Equation 2.8 and Equation 2.11 are together inserted into equation 2.4 to solve for the loss term. This is shown as equation 2.22, where *Ki* is being used to indicate a specific K for each component in the flow path. This does assume all components and tubing are in series, that *L* represents the total length of tubing between the tank and thruster, and that *f* and *D* are constant in all tubing.

$$\Delta P_{loss} = \frac{\rho u^2}{2}\left(\frac{fL}{D} + \sum K_i\right) \tag{2.22}$$

This represents the loss that is being used to modify Bernoulli's equation to determine a thruster inlet pressure. The general form is shown as Equation 2.23. *PInlet* represents the thruster inlet pressure, *PTank* represents the tank pressure, and *ΔPloss* is what's solved for in Equation 2.22.

$$P_{Inlet} = P_{Tank} - \Delta P_{loss} \tag{2.23}$$

2.2 , venturis are tapered orifices that are installed in flight systems to restrict maximum flow rates by intentionally inducing cavitation. As seen in the cross-sectional view in Figure 3.4, they consist of an inlet nozzle, throat, and diffuser. The necessary throat size is specific to each mission, but in every case, the throat size must balance between being small enough to prevent damaging pressure spikes while also large enough to maintain an acceptable pressure loss [46].

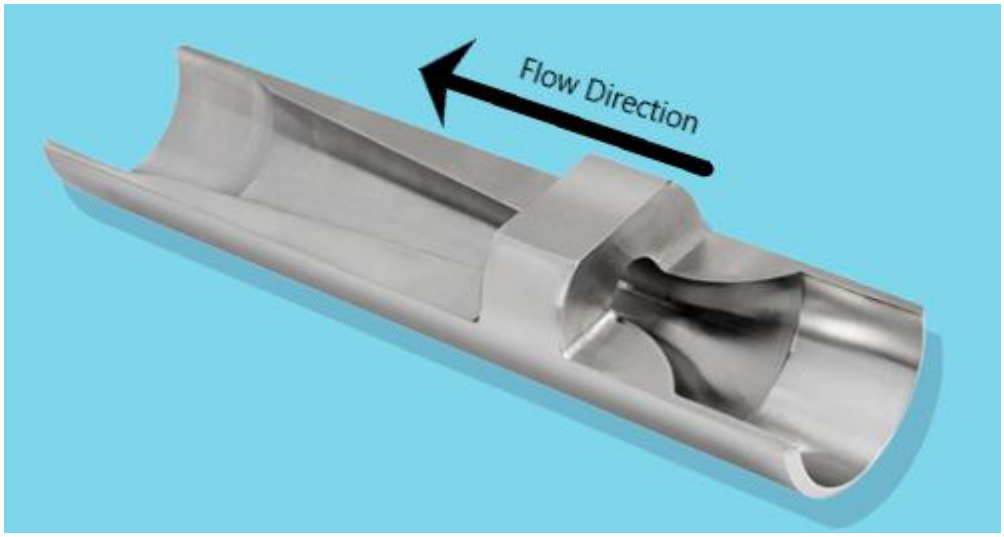

Figure 3.4: Venturi Cross-Sectional View, adapted from [47]

Two venturis were tested with throat diameters of 0.060 in and 0.045 in, both of which fit squarely within the range of standard flight sizes for traditional hydrazine systems; Table 3.3 provides the venturi sizes used on several of NASA's monopropellant hydrazine spacecraft as a reference. The 0.06 in venturi had a wall thickness of 0.035 in, and the 0.045 in venturi had a wall thickness of 0.028 in.

Table 3.3: Venturi Throat Diameters on Previous Monopropellant Missions [33,46,48]

Spacecraft	Venturi Diameters (in)
Global Precipitation Measurement	0.035
	0.043
	0.045
	0.048
Lunar Reconnaissance Orbiter	0.055
	0.075
Plankton, Aerosol, Cloud, ocean Ecosystem	0.052

3.4.3 Filter

Filters are consistently used to prevent contamination of sensitive hardware in both pressurant and propellant lines, making them a staple of in-space propulsion systems. This testing used an 'etched disc' filter, which is one of the most common types due to its low mass and exceptional filtration capabilities. It is constructed of thousands of stacked metallic discs with microscopic, micromachined flow channels, and it can remove contaminants as small as 2 microns [49].

Figure 3.5: Etched Disc Filter [49]

3.4.4 Fill and Drain Valve

Fill and drain valves (FDVs, see Figure 3.6) are another staple of spacecraft propulsion systems since they provide triple redundant sealing and are very adaptable. The primary seal is a metal-to-metal seat that is actuated by turning the hexagonal nut, the secondary seal is the AN cap on the end of the valve, and the tertiary seal is the cylindrical cover, which seals against the black O-ring. Their main function is as an orifice into the propulsion subsystem during ground testing, propellant loading, and other integration and test processes. However, they do not function within the operational system on orbit [50].

Figure 3.6: FDV Example [50]

3.5 Prerequisite Testing

3.5.1 Flow Meter Calibration

The flow meter was originally calibrated for use with water. Applying a correction factor for use with a different liquid than that which a flow meter is calibrated for is a standard practice using Equation 3.1 [51].

$$Q_2 = Q_1 \sqrt{\frac{SG_{Cl}}{SG_{Tl}}} \tag{3.1}$$

However, this only accounts for changes in density, not viscosity, and since GHPB is 21 times more viscous than water, it was not suitable for this test. Consequently, the flow meter had to be re-calibrated for use with GHPB before data collection. This was accomplished by inserting a scale under the catch tank, achieving a steady state flow rate, and then comparing the observed flow rate on the flow meter to the steady-state mass increase on the scale. This was repeated at

various points throughout a range of flow rates representative of testing, then the scale reading was converted to a volumetric flow rate with the propellant's known density. After enough trials, true flow rates as determined by the scale were plotted as a function of flow meter reading and fit with a power trendline. Although flow meter calibration should be independent of the component under test, calibrations were nonetheless completed with all components to verify that the data fell on a single trendline. In total this included 17 trials, each of which is represented by a data point in Figure 3.7. The best fit line, also shown on the plot in Figure 3.7, was then used to correct all observed flow rates.

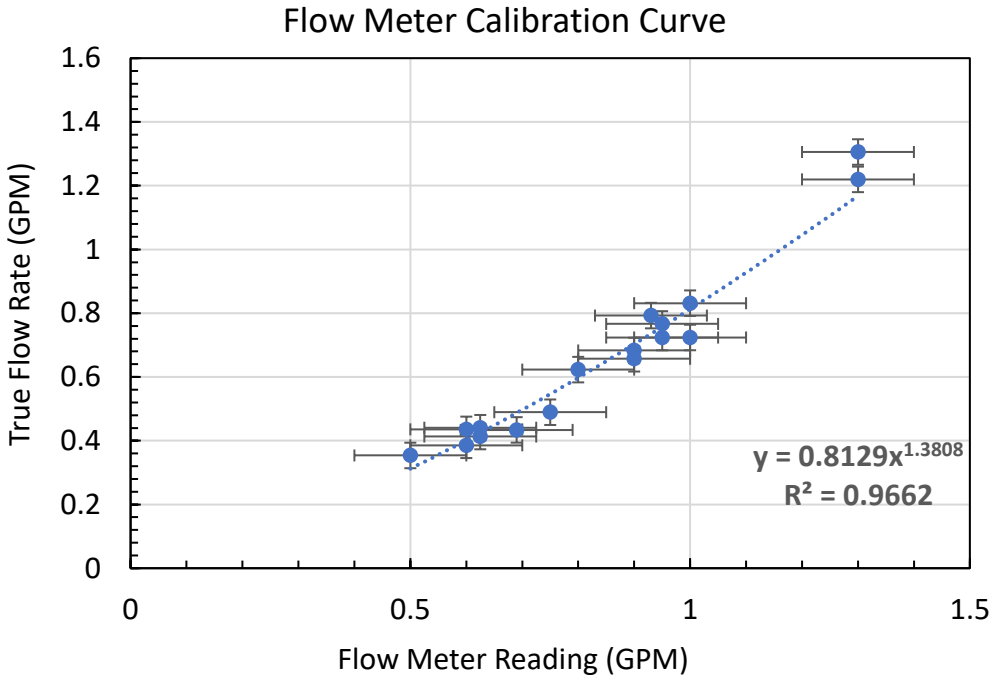

Figure 3.7: Flow Meter Calibration Curve

Note that the maximum observed flow rate was 1.3 GPM, which corrects to a true flow rate of 1.17 GPM on the calibration curve. As depicted on the following data plots, a small percentage of data points were gathered above 1.17 GPM, meaning they had to be extrapolated. However,

recall that from an operational perspective, 1 GPM is an approximate upper limit for flow rates of interest. Additionally, a power law was chosen for this correction in favor of a linear trendline because it offers a higher R^2 within the 0-1 GPM range, but also because the effect of viscosity on a rotameter is non-linear with flow rate. As flow rate increases, the ratio should trend toward unity.

3.5.2 Line Tares

As previously mentioned, all tubing and component interfaces were connected via removable fittings, which disrupted fully develop flow and induced additional pressure losses. These disruptions are not present in an actual spacecraft because these connections are normally joined via orbital welding, which is an automated process without fittings or filler materials that joins tube ends with insignificant flow path disruptions. Removable fittings were only used in this test because welding separate tubing networks for each component would have been impractical. Since the fittings and support tubing produced measurable pressure losses that are not representative of a flight configuration, the losses ‘chargeable’ to the fittings and tubing needed be removed from the analysis. This was done by completing what is known as ‘tare’ testing, which is illustrated in Figure 3.8.

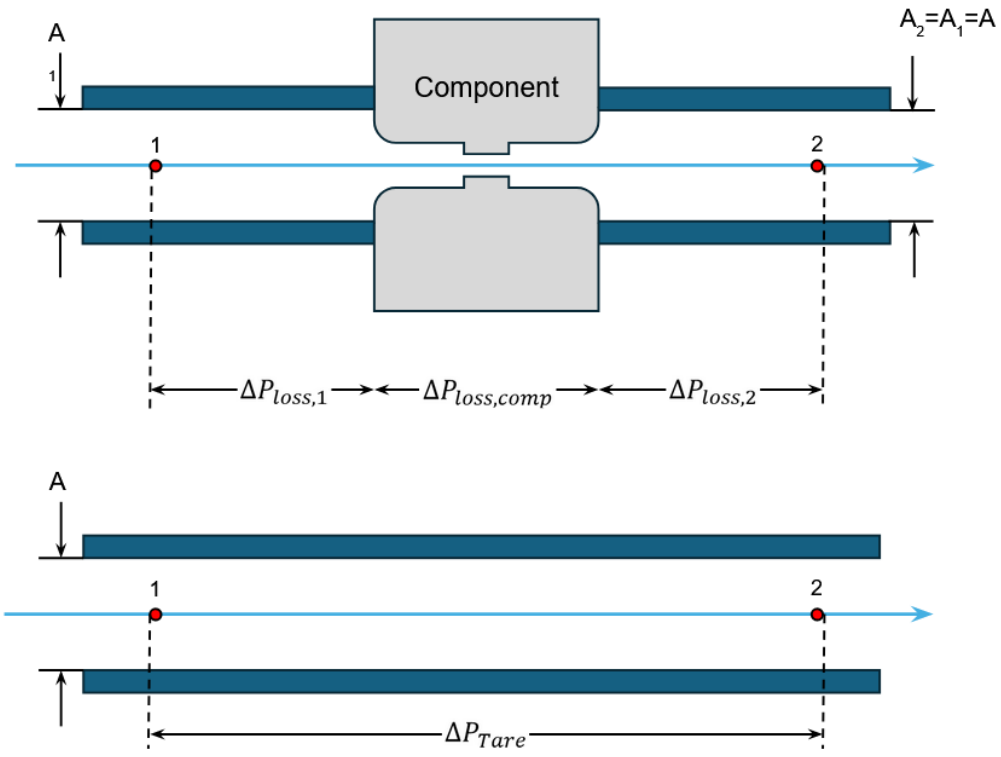

Figure 3.8: Visual Comparison of Tare vs. Component Testing [31]

In the actual setup, there were many fittings installed between stations 1 and 2. As a result, $\Delta P_{loss,1}$ represents the summation of the losses due to fittings and tubing between station 1, where the upstream pressure measurement is taken, and the component itself. $\Delta P_{loss,2}$ measures the same, but from the component to where the downstream measurement is taken at station 2. Together, these are equal to the loss that is not attributable to the component but is being measured by the differential pressure gauge; this is defined as the tare pressure, which is not flight-like and needed to be removed from the data. This is shown mathematically as Equations 3.2 and 3.3

$$\Delta P_{tare} = \Delta P_1 + \Delta P_2 \tag{3.2}$$

$$\Delta P_{measured} = \Delta P_{tare} + \Delta P_{loss,component} \tag{3.3}$$

To measure the loss chargeable to the component alone, ΔP_{tare} needed to be quantified and then removed from the raw data ($\Delta P_{measured}$). To complete this, an empty tube of equivalent length was installed in place of where the flight component (latch valve/filter/venturi) would normally be. Testing was then conducted to measure the differential pressure in the exact same manner it would be if a component was installed. This setup is illustrated in the bottom portion of Figure 3.8, and the result is ΔP_{tare}.

Tare testing was completed for both sized tubes at 300 psi, and the results are plotted in Figure 3.9. Cavitation occurred at 1.62 GPM and 1.42 GPM for the 3/8 in and 1/4 in lines, respectively. Since cavitation would occur in one of the secondary components, such as a hand valve or flow meter, before it occurred in an empty tube, these represent the maximum flow rates achievable with this test equipment.

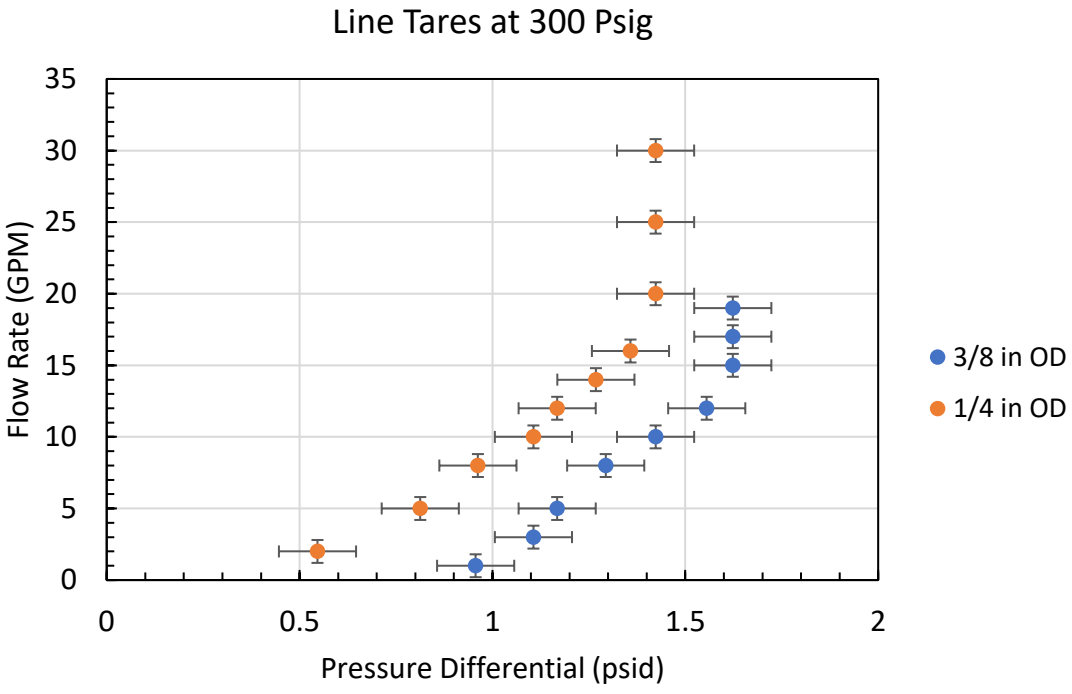

Figure 3.9: Line Tare Flow Testing for 1/4 in and 3/8 in Tubing

For any given flow rate, the tare pressure drop is larger in the ¼ in tube than the 3/8 in tube, which is to be expected. In order to facilitate the raw data correction, the non-cavitating data points were fit with trendlines. These trendlines were second order polynomials, not linear trendlines as might normally be expected. This was because the data provided is used for data reduction, not as a final data product, so the preference was to achieve the highest possible R^2 rather than to allow for extrapolation. However, since a minimum flow rate was needed before the differential pressure gauge produced a measurable response, tare data below the minimum flow rate was fit with an additional, linear trendline as shown in orange. Note that once the flows begin to register on the differential pressure gauge in Figure 3.9**,** the 1/4 in flow reaches cavitation more gradually than the 3/8 in flow. This explains the steeper trendline in Figure 3.10 than Figure 3.11.

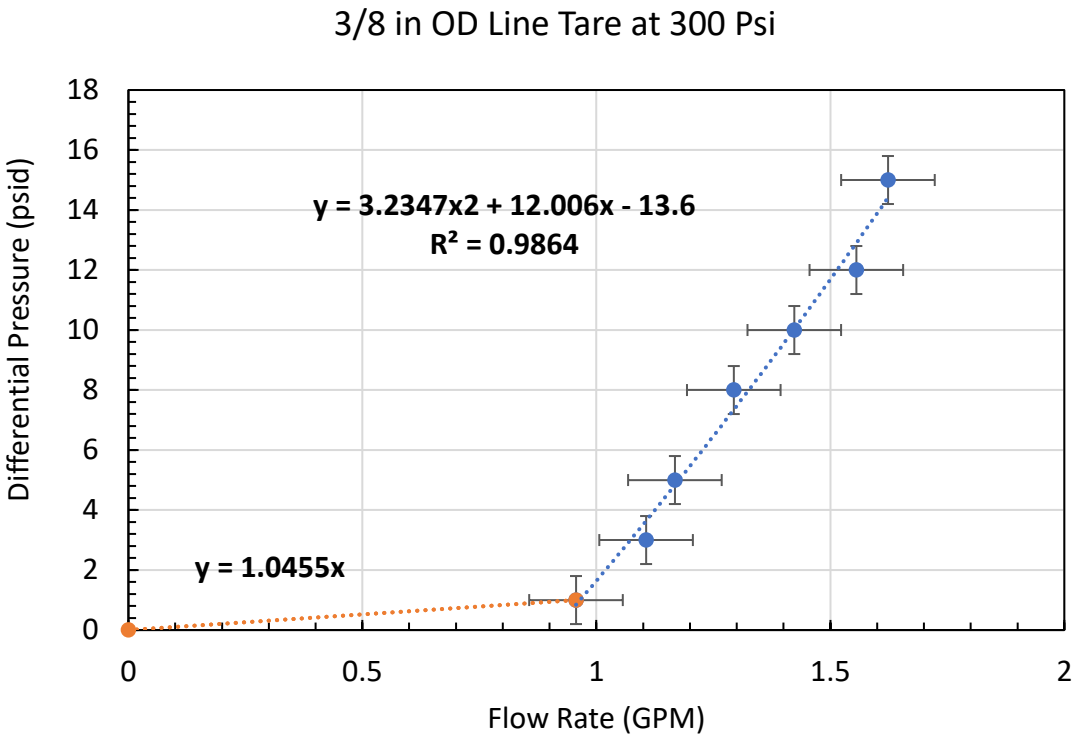

Figure 3.10: 3/8 in OD Tare Correction Trendline

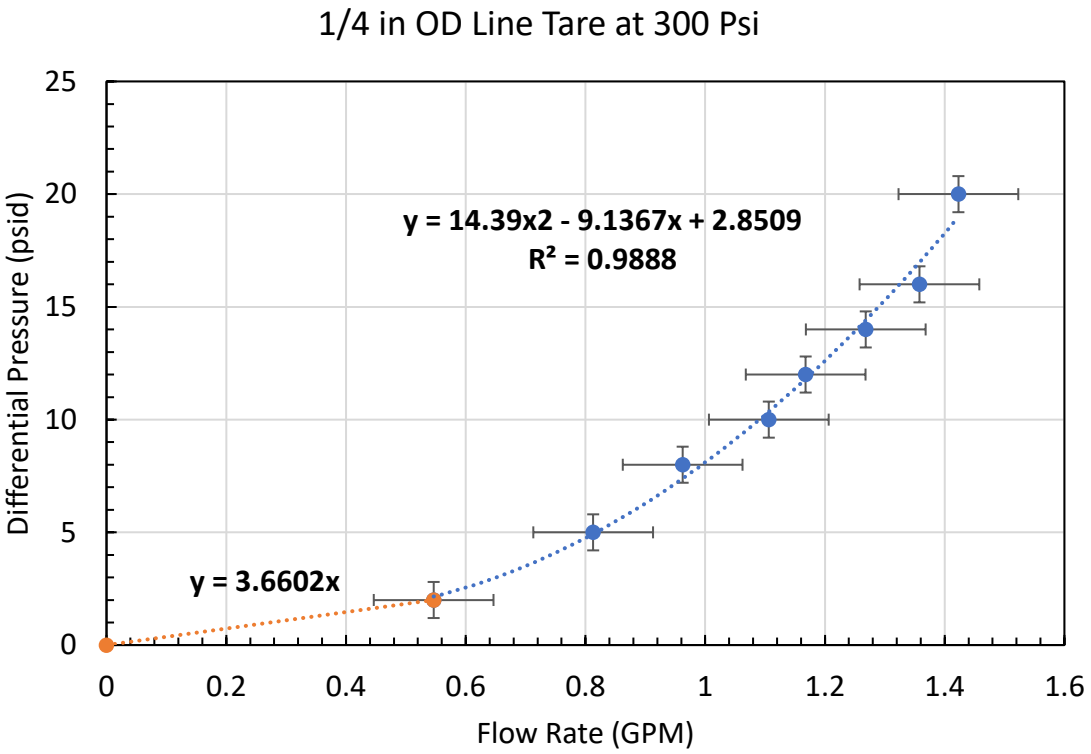

Figure 3.11: 1/4 in OD Tare Correction Trendline

For all plots in Chapter 4:, the raw data have been corrected for flow rate and differential pressure with the trendlines in Figure 3.7 and either Figure 3.10 or Figure 3.11.

Chapter 4: Results

Five components were tested (1 filter, 2 valves, and 2 venturis). Together these components form the backbone of modern propulsion subsystems, making them obvious choices for testing. The only other component that would belong in the same tier of ubiquity as these four components is a thruster valve. However, a thruster valve was omitted for safety reasons because it could not be tested in an unpowered manner.

Having discussed the relationship between ΔP and K in Chapter 2, both are plotted together as functions of flow rate in the following results. Although the pressure loss curves include cavitating flows, recall that cavitating flows are not modeled by K. Therefore, the cavitating data points are reformulated separately as the discharge coefficient results in Section 4.6. Due to their relevance to this chapter, the flow and discharge coefficient equations are repeated below. Note that the variables in this section were converted to SI units, and that K, C_d, and C_{d_o} are all dimensionless. Be advised that due to the relationship between pound-force and its base units not being unity, derivation of the following equations in US customary units will include numerical coefficients.

$$K = \frac{2\Delta P}{\rho}\left(\frac{A}{Q}\right)^2 \tag{2.19}$$

$$C_d = \frac{Q}{A_t}\sqrt{\frac{\rho\beta_t}{2\Delta P}} \tag{2.28}$$

$$C_{d_o} = \frac{Q}{A}\sqrt{\frac{\rho}{2\Delta P_o}} \tag{2.30}$$

4.1 Uncertainty

Note that uncertainty is calculated differently for ΔP and Q than it is for K, C_d, or C_{d_o}. For the pressure loss curves, the uncertainty of any given measurement of each variable (ΔP and Q) is a simple constant in accordance with the accuracies specified in Table 3.1. Therefore, to avoid cluttering the plots, each set of pressure loss curves only has one uncertainty point included. The only exception to this is the filter, since that data set was gathered with different differential pressure gauges depending on driving pressure. As a result, the filter has one uncertainty point specified on each curve.

4.1.1 Uncertainty in K

Unlike the pressure loss curves, the uncertainty in K is a function of both the differential pressure and flow rate measurements at any given point, as well as their respective uncertainties, and it is therefore not constant for any given curve. The uncertainty in a quantity $F(x_1, x_2, \cdots x_N)$ computed from measurements of N parameters whose uncertainties are uncorrelated with each other is given by Equation 4.1 [52].

$$U_Q = \sqrt{\left(\frac{\partial \mathrm{F}}{\partial x_1}\right)^2 * {U_{x1}}^2 + \left(\frac{\partial \mathrm{F}}{\partial x_2}\right)^2 * {U_{x2}}^2 + \cdots + \left(\frac{\partial \mathrm{F}}{\partial x_N}\right)^2 * {U_{xN}}^2} \qquad (4.1)$$

Since $K(Q, \Delta P)$, the uncertainty in K is given by:

$$U_k = \sqrt{\left(\frac{\partial K}{\partial \mathrm{Q}}\right)^2 * {U_{\mathrm{Q}}}^2 + \left(\frac{\partial K}{\partial \Delta P}\right)^2 * {U_{\Delta P}}^2} \qquad (4.2)$$

The uncertainties of the flowmeter, DPG_1, and DPG_2 are ± 0.1 GPM, ± 3 psi, and ± 0.8 psi, respectively (see Table 3.1). From Equations 2.19, 2.28, and 2.30:

$$\frac{\partial K}{\partial \Delta P} = \frac{2}{\rho} * \left(\frac{A}{\mathrm{Q}}\right)^2 \tag{4.3}$$

$$\frac{\partial K}{\partial \mathrm{Q}} = \frac{-4 * \Delta P * A^2}{\rho \mathrm{Q}^3} \tag{4.4}$$

Substituting into Equation 4.2 gives:

$$U_K = \sqrt{\left(\frac{U_{\Delta P} * 2A^2}{\rho Q^2}\right)^2 + \left(\frac{U_{\mathrm{Q}} * 4 * \Delta P * A^2}{\rho Q^3}\right)^2} \tag{4.5}$$

Note that the flow rate is cubed and squared in the two denominators. This caused U_k to be very large at low flow rates, and then rapidly decrease with increasing flow rate. This trend exists regardless of propellant choice. However, it is particularly relevant to this test because when coupled with the crude flow meter that was used, it has the effect of exacerbating the low flow rate uncertainty.

4.1.2 Uncertainty in C_d

The same process is used to calculate the uncertainty in C_d (U_{Cd}). As mentioned at the conclusion of Section 2.2, once the flow is cavitating and therefore decoupled from the downstream pressure, the pressure differential is measured with respect to the throat. Since the pressure at throat is less than or equal to the propellant vapor pressure, which is insignificant by comparison to the driving pressure, ΔP is approximately equal to the driving pressure. Therefore, the uncertainty in ΔP is driven by the accuracy of the standard pressure gauge, not the differential

pressure gauge that was used for U_K. This value was also provided by the manufacturer and given in Table 3.1 as ± 3 psi. Substituting Equation 2.28 into Equation 4.1 gives:

$$U_{C_d} = \sqrt{\left(\frac{\partial C_d}{\partial \mathrm{Q}}\right)^2 * {U_\mathrm{Q}}^2 + \left(\frac{\partial C_d}{\partial \Delta P_{vp}}\right)^2 * {U_P}^2} \tag{4.6}$$

The sensitivity coefficients are given by:

$$\frac{\partial C_d}{\partial \Delta P} = \frac{-Q\sqrt{\rho\beta_t}}{2A\sqrt{2\Delta P^3}} \tag{4.7}$$

$$\frac{\partial C_d}{\partial \mathrm{Q}} = \frac{\sqrt{\rho\beta_t}}{A\sqrt{2\Delta P}} \tag{4.8}$$

This leads to the final form of U_{Cd}, shown as Equation 4.9. The expression for the uncertainty in C_{d_o} can be determined by setting $\beta = 1$. This was therefore not derived separately, but it is shown as Equation 4.10.

$$U_{C_d} = \sqrt{\left(\frac{U_Q\sqrt{\rho\beta}}{A\sqrt{2\Delta P}}\right)^2 + \left(\frac{-QU_P\sqrt{\rho\beta}}{2A\sqrt{2\Delta P^3}}\right)^2} \tag{4.9}$$

$$U_{C_{d_o}} = \sqrt{\left(\frac{U_Q\sqrt{\rho}}{A\sqrt{2\Delta P}}\right)^2 + \left(\frac{-QU_P\sqrt{\rho}}{2A\sqrt{2\Delta P^3}}\right)^2} \tag{4.10}$$

4.1 Venturis

As can be seen from Figure 4.1, the 0.060 in venturi produced cavitation for the 100 psi and 200 psi flows at 0.93 GPM and 1.17 GPM, respectively, but it did not cavitate for the 300 psi run. This is not unexpected, as a higher driving pressure requires a larger acceleration to reach the

fluid's vapor pressure. As a result, flows with higher driving pressures cavitate at higher flow rates, assuming all other variables are constant.

As anticipated, both ΔP and K are much larger than would have been expected for a similar hydrazine system. It is also seen that when Q > 0.8 GPM, K is approximately independent of the flow rate. Although the exact flow rate at which this occurs is specific to each propellant and component being tested, the overall trend of K approaching a constant value with increasing flow rates is consistent with hydrazine data as well. The trends in both magnitude of K and its dependence on flow rate are seen in all other plots. A thorough discussion on quantifying the disparities between these results and expectations with hydrazine is reserved for Chapter 5

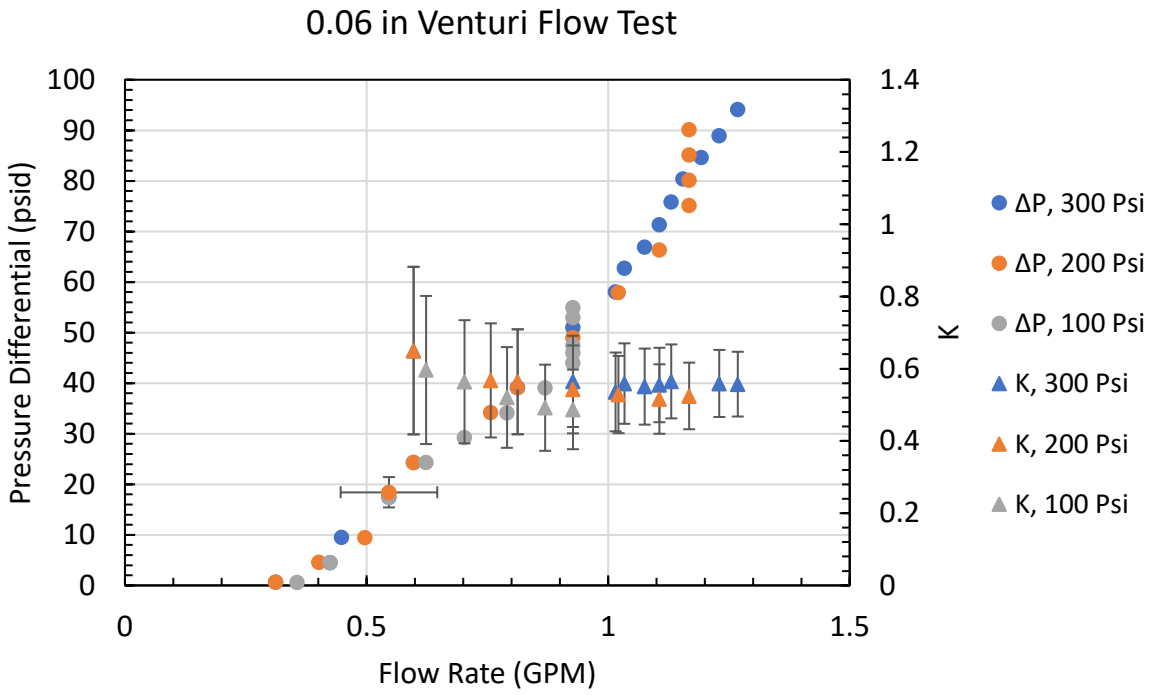

Figure 4.1: Flow Test for 0.06 in Venturi

Figure 4.2 shows cavitation in the 0.045 in venturi for all three driving pressures. Cavitation occurred at 0.55 GPM, 0.75 GPM, and 0.93 GPM at driving pressures of 100 psi, 200 psi, and 300

psi, respectively. Note that the 0.045 in venturi's cavitation flow rate at 300 psi is equivalent to the 0.060 in venturi's cavitation flow rate at 100 psi, corroborating the intuitive relationship between smaller throat diameters and greater flow acceleration, thus leading to greater reductions in static pressure and lower maximum flow rates.

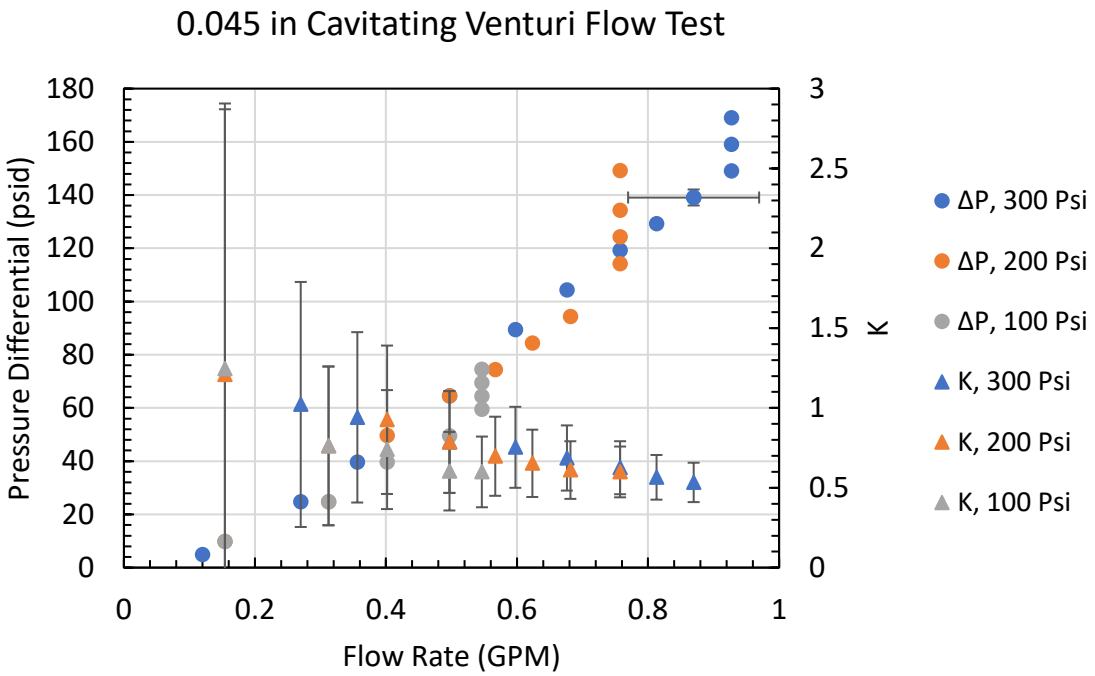

Figure 4.2: Flow Test for the 0.045 in Venturi

4.2 Filter

As discussed in Chapter 3.3 Data Acquisition Hardware, two different DPGs were used depending on the range of expected pressure drops. For the filter, this meant the 200 psi and 300 psi flows used a different gauge than the 100 psi and 50 psi flows. This does result in a small downward shift of the high-pressure curves from the trend established by the low-pressure curves. This is visible near the 22 psid mark, but within the uncertainty band (± 3 psi) of the differential pressure gauge used for the 200 and 300 psi flows.

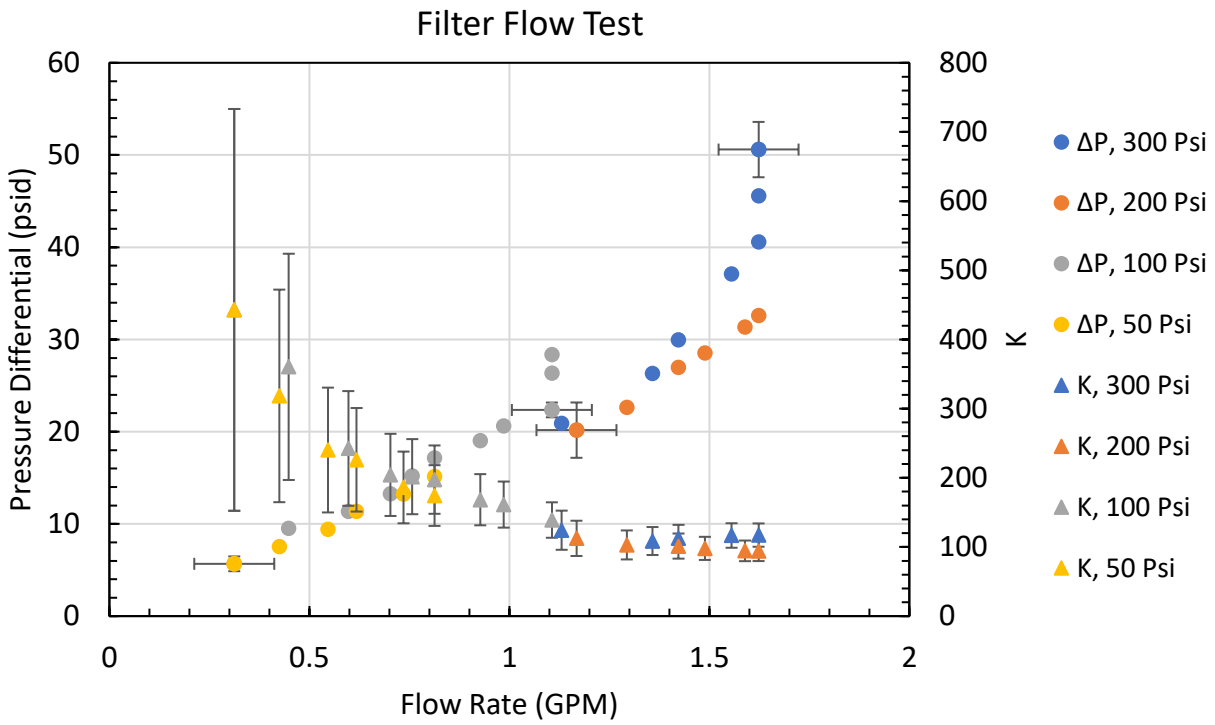

Figure 4.3: Filter Flow Test

At 50 psi, the flow reached a maximum of 0.81 GPM but did not cavitate. At 100 psi, the flow cavitated at 1.10 GPM. Recall that the filter was a 3/8 in component, and as discussed during evaluation of Figure 3.9, 1.62 GPM is the maximum flow rate achievable for the 3/8 in setup because cavitation occurs elsewhere in the system at this flow rate. This is evidenced in the plot, which shows both the 200 and 300 psi flows reaching the same maximum flow rate of 1.62 GPM. Consequently, the filter's cavitation flow rate can only be concluded to be greater than or equal to 1.62 GPM at these driving pressures. This is a sufficient result since the filter has a large effective throat size, and assuming there is an appropriately sized venturi somewhere else in the system, in practice it would not be expected or ideal for it to cavitate. Since the filter's cavitation flow rate is known for the 100 psi driving pressure to be 1.10 GPM, by comparison to Figure 4.1, the filter can

be stated to have an effective throat diameter greater than 0.06 in. Additionally, K for the filter becomes approximately independent of Q around 1.2 GPM.

4.3 Fill & Drain Valve

Given their exclusion from the actual flight operations, the only situation where pressure loss across a liquid FDV is relevant is when loading propellant onto the spacecraft. Since this is a low-pressure operation, the FDV only needed to be tested at a driving pressure of 50 psi to encompass realistic flow rates. For this test, the FDV reached a maximum flow rate and pressure drop of 0.81 GPM and 9.06 psid respectively, but it did not cavitate. As a result, its effective throat diameter cannot be stated conclusively, although it can be inferred from the mild pressure losses to be a relatively large percentage of the actual throat diameter. Even without knowing the internal dimensions, a large effective throat area, mild pressure drop, and lack of cavitation are all expected due to the simple geometry of the valve. Furthermore, K is independent of Q within the measurement uncertainty for the flow rates tested.

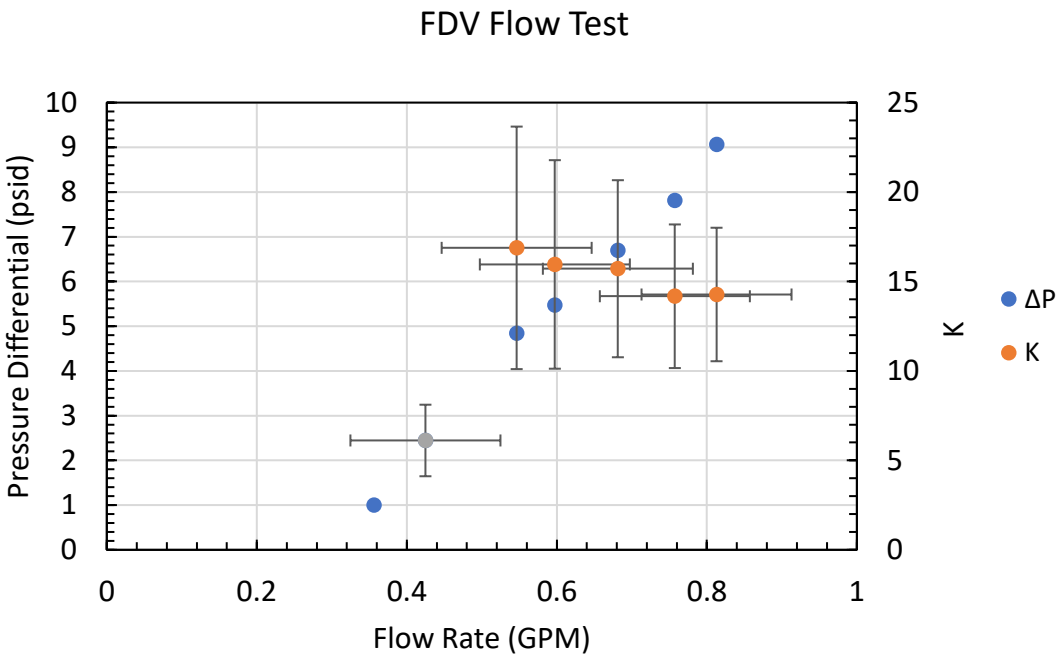

Figure 4.4: Flow Test for FDV

4.4 Latch Valve

A flight latch valve was tested at driving pressures of 50 psi, 100 psi, 200 psi, and 300 psi. Run times were shorter than other components because it was the first component to be tested and the process was still being sorted out. As a result, several trials were completed at each driving pressure to ensure that enough data were gathered despite the short duration tests. This explains the higher quantity of data points by comparison to the rest of the components. Each of the other components only received a single trial at each driving pressure since that was sufficient to capture the entire flow curve through its maximum flow rate. As can be seen in Figure 4.5, the latch valve reached a maximum flow rate of 0.79 GPM at 50 psi but did not cavitate, and at 100 psi it began to cavitate at 0.93 GPM. At 300 psi, cavitation is seen at 1.36 GPM. Unfortunately, the test at 200 psi ran out of propellant before reaching cavitation. Based on the trends shown in the 100 and 300

psi flows, an approximate cavitation flow rate for the 200 psi flow would be 1.1 GPM, although this cannot be stated conclusively. Furthermore, K becomes approximately independent of Q around 0.9 GPM.

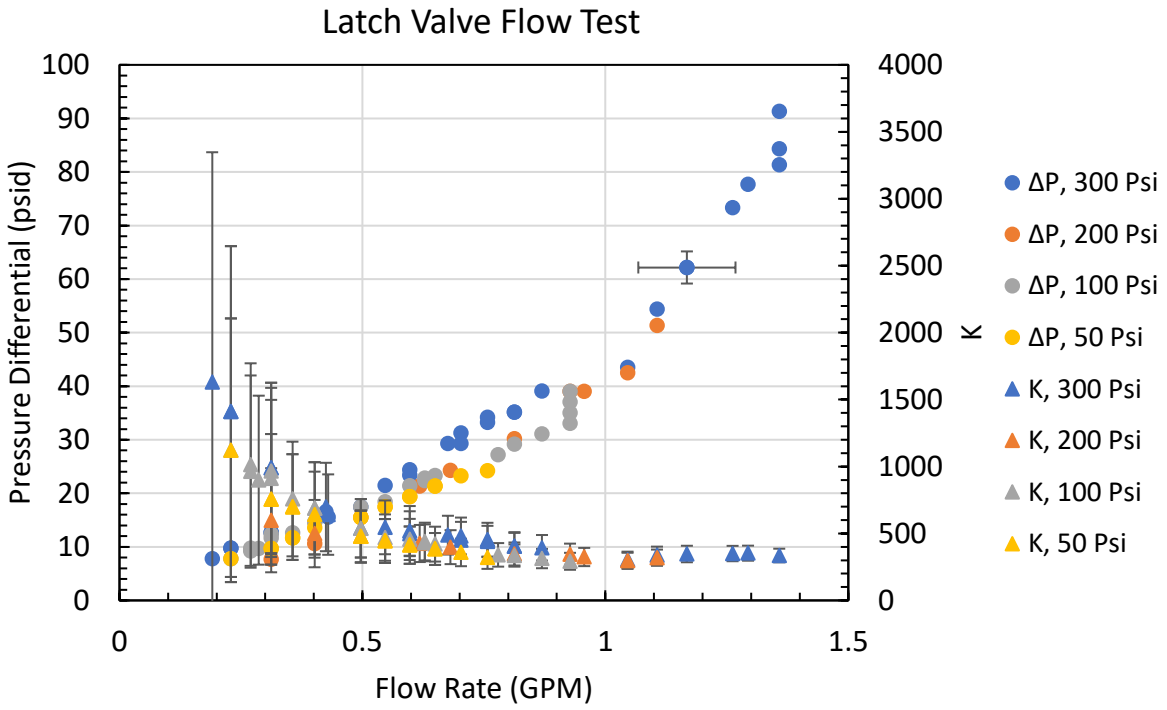

Figure 4.5: Latch Valve Flow Test

Recall that a component's 'effective' throat area is the venturi size that would produce an equivalent cavitation flow rate. Since both the latch valve and the 0.060 in venturi cavitated at 0.93 GPM for a driving pressure of 100 psi, the latch valve can be said to exhibit an effective throat diameter of approximately 0.06 in. Without knowing the actual throat diameter of the latch valve, it can be assumed to be significantly larger than 0.06 in. As an example, the latch valve can be assumed to have an actual throat area of 0.12 in. That would mean the latch valve's effective throat area is 50% of its actual throat area, implying that the viscous interactions within the valve's internal flow path caused a substantial deviation from the ideal flow.

4.5 Water Approximation

As shown in Table 2.1, hydrazine and water have very similar densities and viscosities. It was previously mentioned that due to these similarities, water is often used as a substitute for hydrazine when testing propellant systems. The equations used to correct the pressure loss for differences in density or density and viscosity are presented below [38]. In the equations, ΔP_C represents the corrected pressure drop, and ΔP_{tl} represents the pressure drop measured with the test liquid. The dynamic viscosity of each liquid is represented by μ, and the specific gravity is represented by *SG*, each of which uses the same subscript notation as *ΔP*.

$$\Delta P_C = \Delta P_{tl}\left(\frac{SG_C}{SG_{tl}}\right) \tag{4.11}$$

$$\Delta P_C = \Delta P_{tl}\left(\frac{\mu_C}{\mu_{tl}}\right)^{0.25}\left(\frac{SG_C}{SG_{tl}}\right)^{0.75} \tag{4.12}$$

Figure 4.6 compares measurements in the latch valve with GHPB to measurements made by the valve vendor with water. The results show that Equations 4.11 and 4.12 do not do a good job of predicting pressure losses with GHPB from measurements with water in the same valve and under similar conditions. This is because Equations 4.11 and 4.12 assume *K* is independent of the liquid when, in fact, it is not.

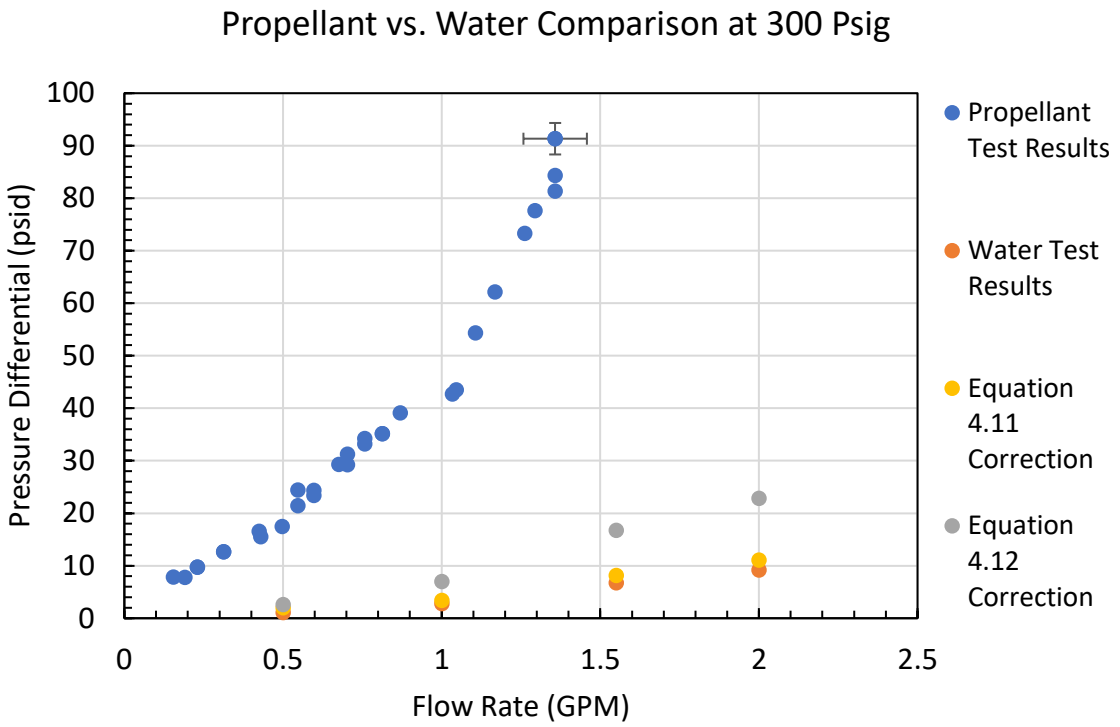

Figure 4.6: Pressure Drop through a Latch Valve with GHPB (measured in this work) and Water (measured by the latch valve manufacturer)

4.6 Discharge Coefficient Results

Figure 4.7 provides the C_d for all venturi flows that cavitated, and likewise the C_{d_o} for the latch valve and filter flows that cavitated. The error bars are symmetric about each point, but since C_d must be less than or equal to 1, the positive error bars for the 0.045 in venturi are truncated. Additionally, note that both the coefficient (Equation 2.28) and uncertainty (Equation 4.9) calculations each have an area term in the denominator, which is much larger for both the filter and latch valve than the venturis. This explains the discrepancy in magnitudes between the venturis and non-venturi components, and it is also why non-venturi components are sometimes classified by their 'C_dA'. Furthermore, the exact throat area was not available for either the filter or latch valve, so they were both estimated to be circular with diameters of 0.12 in. This is double the

effective throat diameter of the latch valve that was determined in Chapter 4.4. The approximations associated with these two components are acceptable because unlike the venturis, neither of these components would ever be designed to actually cavitate in flight. Therefore, C_{d_o} for the filter and latch valve would never be actual design parameters, and are only included in Figure 4.7 for completeness.

The results show that within the bounds of their uncertainties, the discharge coefficients are independent of the flow rate and approximately equal in magnitude to the values expected with hydrazine.

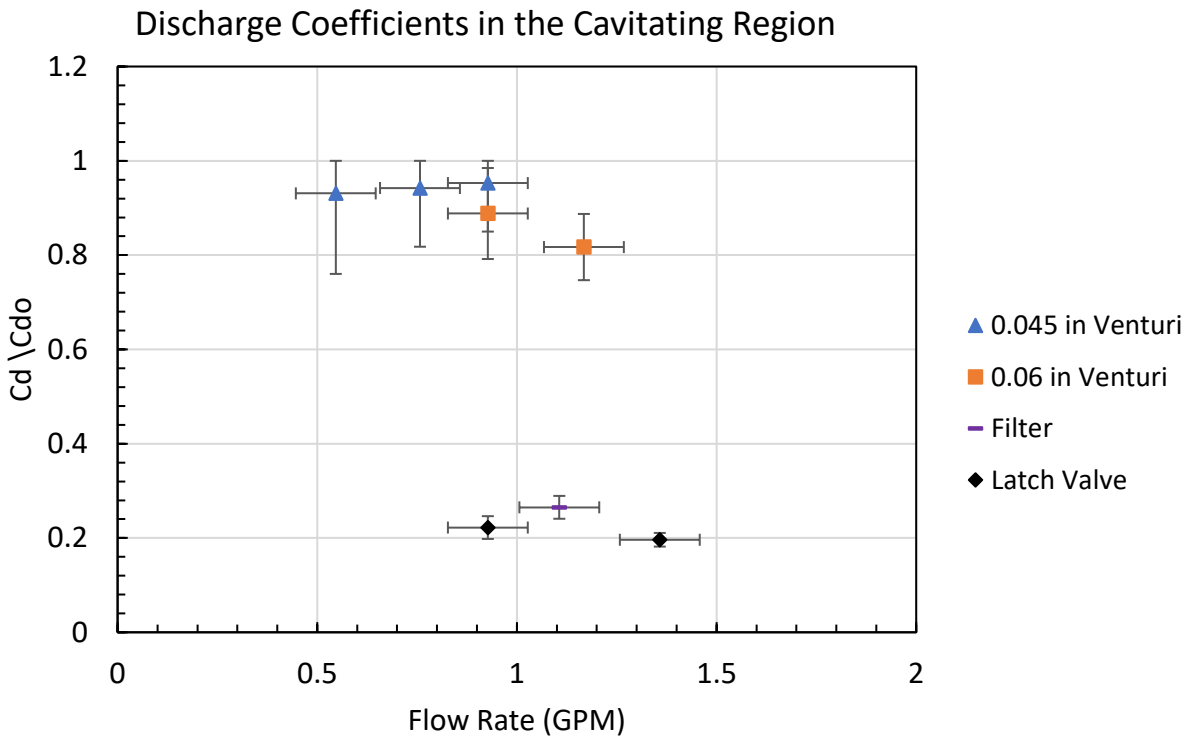

Figure 4.7: Discharge Coefficient for Cavitating Flows with Uncertainties

4.7 Material Compatibility

One of the most important considerations for any new propellant is whether it is compatible for long term exposure with materials that are common in propulsion systems and ground support equipment. Although material compatibility testing was not an official goal of this work, since the experiments were completed over the course of 3 weeks, the experiments amounted to a 3-week exposure test with common propulsion system materials. The results are relevant to the flow tests because incompatibilities could affect the data – especially if there was any solid particulate generation. No unexpected pressure or temperature rises were observed during the experiments that would indicate a reaction between the propellant and materials. A post-test inspection of the component internal flow paths showed no visible changes. Therefore, it does not appear that material incompatibilities were present.

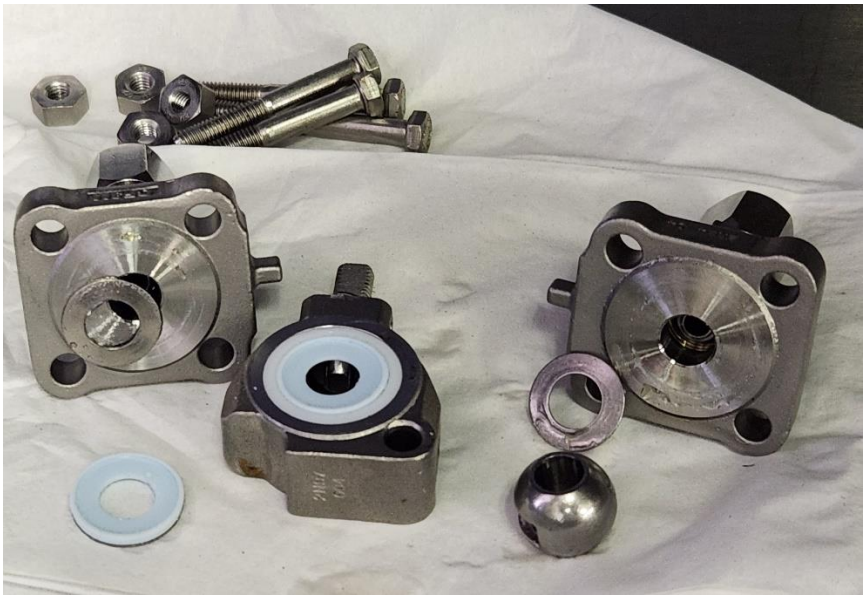

Figure 4.8: Hand Valve Disassembled Post-Test Showing No Signs of Reaction

4.8 Process Errors

The uncertainties previously calculated for the loss and discharge coefficients only consider the errors from the instrumentation; however, there are potential sources of systematic error in the test process that should be considered as well, at least qualitatively. The primary error source involved human interpretation of the analog instrumentation's readings. Without an automated data collection process, data were gathered periodically by reviewing videos of the instrument dials, which could also introduce small errors due to camera angles. Since multiple runs were completed on the latch valve for each driving pressure, this can be partially analyzed by evaluating how repeatable the data sets are. Figure 4.9 shows three runs at 300 psi, but there were multiple runs at 200 psi, 100 psi, and 50 psi as well. For all four cases, a second order polynomial can be fit with an R^2 greater than 0.98 between the data sets.

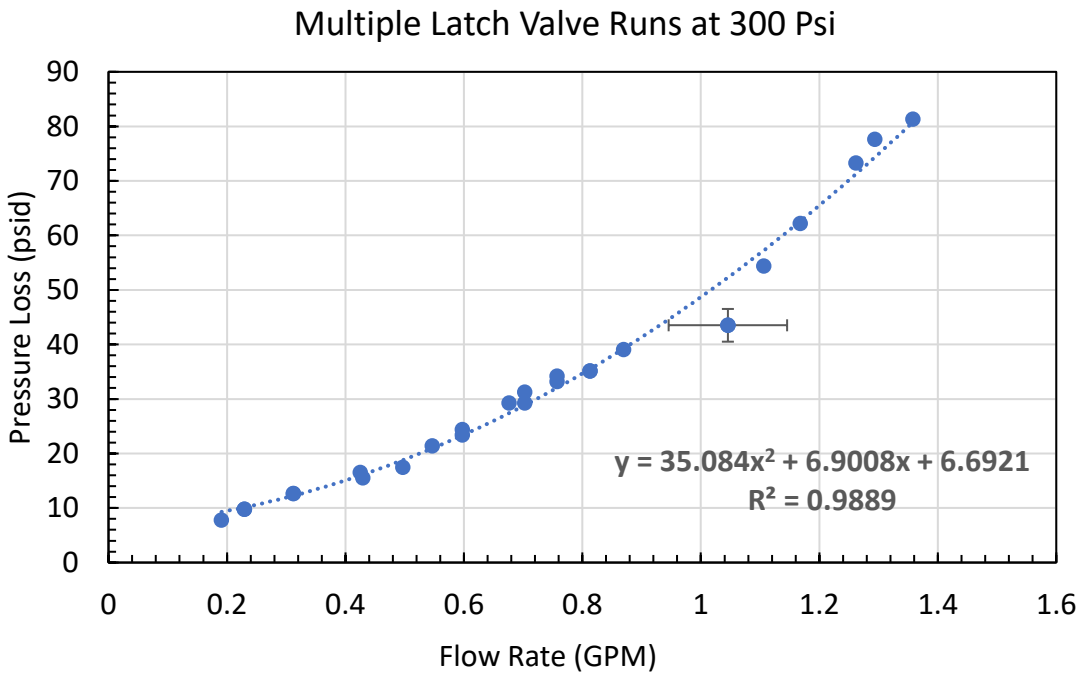

Figure 4.9: Individual Latch Valve Runs at 300 Psi

A repeatable process does not necessarily imply accuracy, so it is conceivable that a systematic error was applied throughout the data. However, an error from the camera angle with respect to the dials would need to have been smaller than ±0.1 GPM or ±1 psi to be imperceptible to the operators. Given that the test was intended to illustrate large disparities between this propellant and traditional hydrazine, an error that is within the bounds of what the operators could not visually perceive is acceptable and within expectations for analog data collection.

Additional error was introduced by the pressure regulator, which did not have a sufficient flow capability to overcome the conversion of static pressure into dynamic pressure as the propellant began to flow. Consequently, propellant pressure at the inlet to the test section, as measured by G1 in Figure 3.1, consistently showed some degree of reduction in driving pressure. The precise amount varied with flow conditions, but never exceeded 30 psi.

There is not an established level of uncertainty required for this test since the data will be used for design processes on missions with varying certainty requirements. In all cases, the uncertainty would need to be enveloped by the design margin applied. Therefore, some missions may find the fidelity of this data sufficient, while others require less uncertainty.

Chapter 5: Comparison to Mission Precedent

To contextualize the effectiveness of GHPB as a ‘drop-in’ replacement, the data can be used to predict performance on an actual monopropellant mission. Before doing so though, context must be provided about standard spacecraft propulsion architecture. Most spacecraft are ‘pressure-fed’. This means that the motive force on the propellant comes from pressurized gas – usually helium or nitrogen – instead of a turbopump. These pressure-fed systems are broadly classified as either ‘regulated’ or ‘blowdown’. In a regulated system, the propellant and pressurant are stored in separate tanks with a pressure regulator between them that maintains the propellant tank at a constant pressure. As a result, regulated systems store ample gas to maintain a constant flow rate throughout the life of the mission. On the other hand, a blowdown system stores both propellant and pressurant in the same tank. As propellant is expelled, the finite amount of gas expands to fill the larger volume, which causes the driving pressure of the propellant to decrease over time [53]. This change in driving pressure causes propellant flow rates to change (decrease) over the duration of the mission. Monopropellant systems are more often blowdown than pressure regulated, and since GHPB is currently being marketed for monopropellant systems, this analysis will focus on the blowdown architecture. The blowdown architecture also provides a more conservative analysis as it pertains to pressure losses since the total pressure available is finite. Figure 5.1 provides a simplified example schematic to illustrate the differences between pressure-regulated and blowdown architectures.

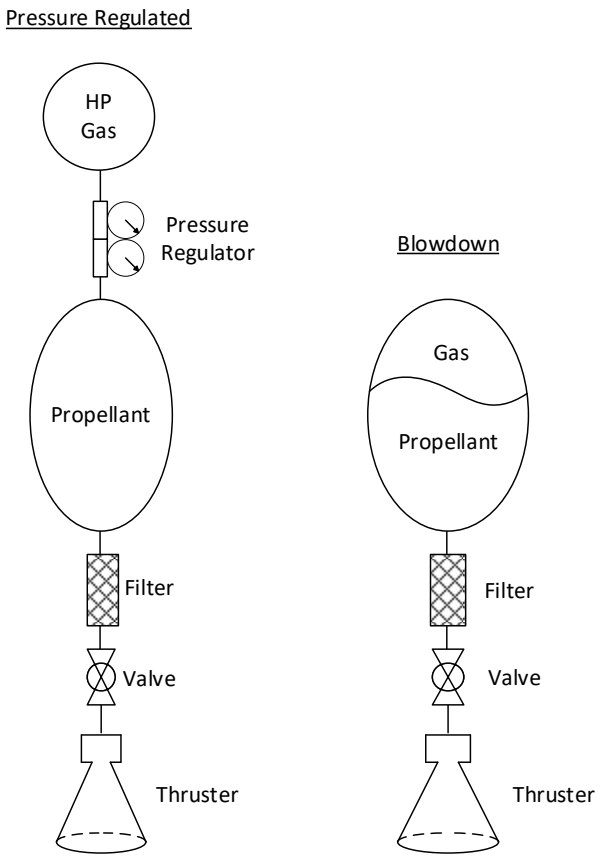

Figure 5.1: Simplified Example Schematics for a Regulated and Blowdown System

Figure 5.2 is a schematic illustration of the propulsion subsystem for NASA's Plankton, Aerosol, Cloud, ocean Ecosystem (PACE) mission. It is a 'standard' hydrazine blowdown design, where the pressure at the inlet of any thruster valve is the tank pressure minus the losses across a latch valve, filter, and venturi. Even though the schematic shows two latch valves and venturis (one for each bank of thrusters), the two thruster banks are for redundancy (ie. fault tolerance) and only one bank operates at a time. Therefore, the model considers only one latch valve and venturi. Note that there would also be an additional pressure loss across the (dual-seated) thruster inlet valve (shown by the 'X's at the inlet of the thruster), but no thruster valves were included in this test since they require power to operate. Therefore, the test data were used to sum losses up to the valve, but not across.

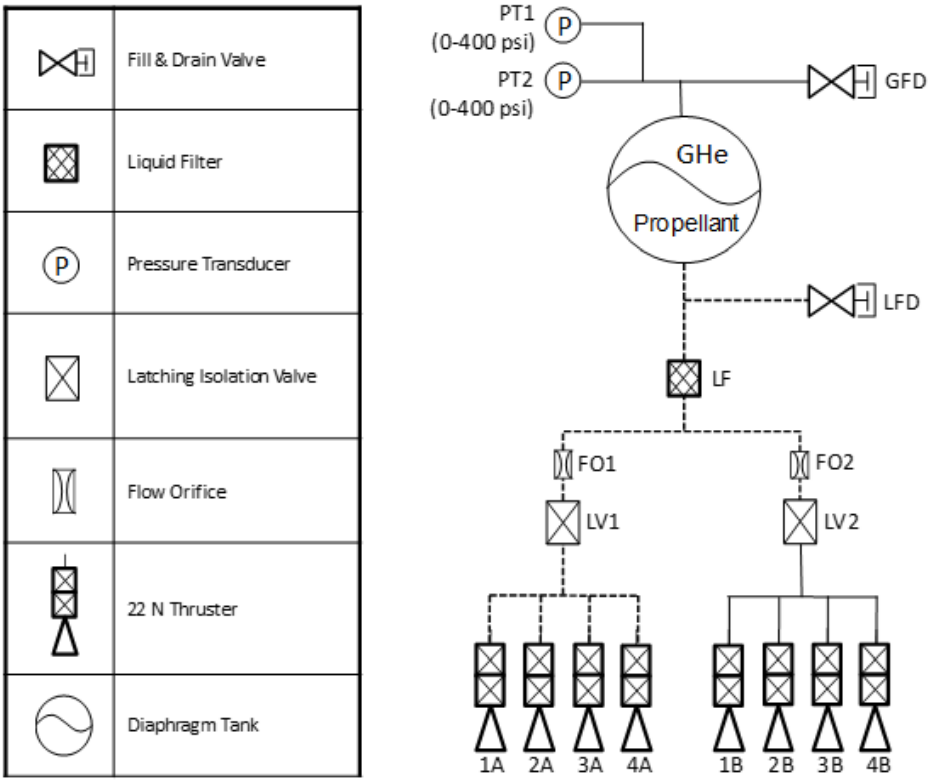

Figure 5.2: PACE Propulsion Subsystem Schematic [46]

Figure 5.3 provides a visual representation of the pressure losses occurring on PACE as propellant flows from the tank to the thruster. A standard minimum thruster inlet pressure is 75 psi [54], meaning the lower bound is fixed by the thruster design capabilities. The upper tank limit is chosen to be 400 psi to match the maximum pressure transducer readings on PACE (refer to Figure 5.2), but 400 psi is also a good representative of a standard maximum tank pressure [55]. Therefore, to avoid costly tank requalification procedures associated with raising the maximum tank pressure, the upper bound on Figure 5.3 is also fixed. The challenge with GHPB is succinctly stated as remaining within the upper and lower bounds, despite the increased pressure losses, without sacrificing total thrust output (ie. performance).

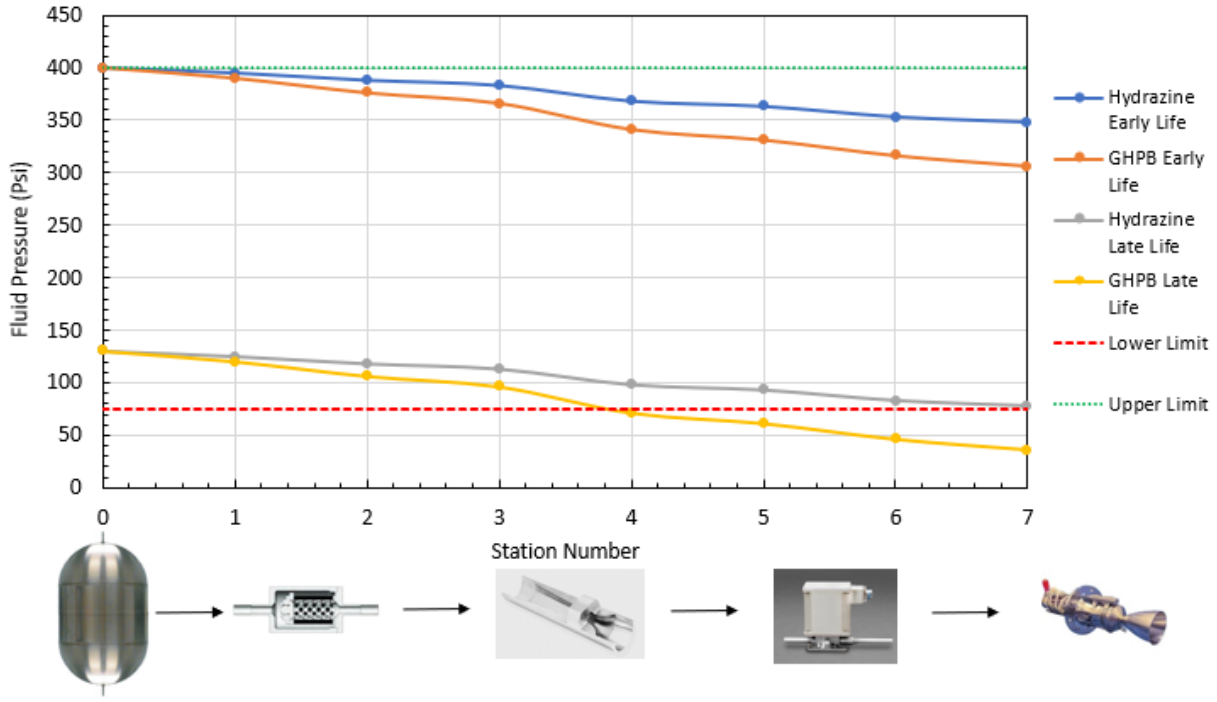

Figure 5.3: Pressure Losses Along the PACE Flow Path

Figure 5.3 is provided as a graphical representation of the losses induced, rather than a quantitative analysis (which is provided in the subsequent three sections), so the plot lengths and slopes are not to scale. Each station represents the inlet our outlet of a component in the PACE feed system. The arrows indicate major losses due to friction between the propellant and tubing in between the components. Since these losses are mild, they are represented by a gradual slope. On the other hand, the losses across the components are larger and are therefore represented by steeper slopes. The purpose of determining K for each component, and therefore the purpose of this work, is to allow the slopes across the components to be determined. As shown in the figure, at the beginning of life (BOL) there is usually plenty of margin, even despite the larger losses produced with GHPB. However, towards the end of life (EOL), there will necessarily be a starting tank pressure for which hydrazine stays within bounds, but GHPB does not. All else equal. the practical impact of this would be that PACE would need to perform the EOL deorbit maneuver sooner if it

used GHPB, therefore achieving a shorter mission life. To fully understand the performance differences between GHPB and hydrazine, the two limiting cases (BOL & EOL) must be quantified. The relevance of the BOL flow rate is that since it is also the maximum flow rate, it will provide the largest pressure drop. Holding all other variables constant, it will also be the point of the largest disparity between the two propellants. The EOL flow rate and pressure loss must also be considered to ensure that the EOL thruster injection pressure is within the thruster's operating bounds. This is vital for ensuring that spacecraft can perform EOL de-orbit maneuvers. It would be prudent to ensure the spacecraft has thruster capabilities throughout the life of the mission regardless, but EOL thruster performance is especially scrutinized because it is imperative that spacecraft can perform de-orbit maneuvers to prevent further proliferation of orbital debris.

5.1 Beginning of Life

Surge testing analysis done for the PACE propulsion subsystem showed a maximum flow rate of 0.156 lbm/s with a tank pressure of 385 psi and a 0.048 in venturi [46]. Since surge flow rates are transient and higher than operational flow rates, a sensible estimate for PACE's initial operational flow rate is 0.1 lbm/s, or 0.71 GPM for hydrazine.

Although the exact part numbers of the filter and latch valve on PACE are not specified, it is reasonable to assume they are very similar to the currently available industry hardware. As a result, the pressure loss and flow rate data that Vacco makes public in their latch valve and filter catalogs can be used to determine a loss coefficient for each component with hydrazine. The part numbers are V1E10453-01 and F1D10397-04 for the latch valve and filter, respectively. While the latch valve data have pressure drops across a range of flow rates (including 0.1 lbm/s), the filter only has one data point at a flow rate of 0.19 lbm/s [49,56]. Since K is unknown function of Q, it

is not clear how to extrapolate the manufacturer's pressure loss to 0.1 lbm/sec. However, since the filter's predicted loss is only 1.6 psi at 0.19 lbm/s, whatever the loss at 0.1 lbm/sec turns out to be, it will be much smaller than other losses and thus is acceptable for this use.

Since similar flow test data are not available for the venturis, an estimate for K_t can be determined from control-volume theory for sudden contractions and expansions. This is shown in Equations 5.1 and 5.2, where both are derived from conservation of mass, momentum, and energy for constant-density steady flow. Equation 5.1 is for sudden contractions and Equation 5.2 is for sudden expansions [31].

$$K_{t_{SC}} = \frac{1}{2}\left(1 - \frac{{D_t}^2}{ID^2}\right) \tag{5.1}$$

$$K_{t_{SE}} = \left(1 - \frac{{D_t}^2}{ID^2}\right)^2 \tag{5.2}$$

The total loss across the venturi can be treated as the sum of the losses in the contracting and expanding sections. However, since these equations are for sudden changes, they need to be modified to reflect the fact that both the contractions and expansions are gradual. Empirically determined correction factors exist for gradual changes, and they are shown as Equations 5.3 and 5.4. Although the half angles are not known for the venturis, they can be determined from external measurements and basic geometry.

$$C_C = 1.6 \sin\left(\frac{\theta_C}{2}\right) \tag{5.3}$$

$$C_E = 2.6 \sin\left(\frac{\theta_E}{2}\right) \tag{5.4}$$

This leads to the final form of the K_t estimates, as shown in Equation 5.5. Note that Equations 5.3 and 5.4 only hold for angles less than 45°, and they each have different forms for larger angles [31]. In this case, the convergence and divergence angles for the 0.045 in venturi were 17° and 3.93°, respectively. For the 0.06 in venturi, they were 15° and 3.71°, respectively. It is clear that the contraction angle is much larger than the expansion angle for both venturis, which was also illustrated in Figure 3.4. This is because the process of converting static pressure to velocity during a contraction is much more stable than the opposite process during an expansion. As a result, when a contraction is followed by an expansion with equal half angles, the loss in the expansion dominates [37]. In order to combat this and minimize the total loss across the venturi, the expansion section has a significantly smaller half angle than the contraction.

$$K_t = C_C K_{t_{SC}} + C_E K_{t_{SE}} \tag{5.5}$$

Notably, the equation for K_t is not a function of flow rate, just the flow geometry. This conflicts with the results in Chapter 4.6, which showed all components to be dependent on flow rate. Although that was true for the venturis, due to their higher flow rates they showed much less dependence on flow rate than the latch valve and filter did. This dependence should also be lessened in the hydrazine system, as the lower viscosity will increase flow rates across the board. Consequently, this is accepted as an approximation. The results for all K values in PACE's hydrazine system are compiled in Table 5.1.

Table 5.1: Predicted K Values for the PACE Hydrazine System

Component	Corresponding Flow Rate (lbm/s)	K	K_t
Latch Valve	0.1	30.51	-
Filter	0.19	8.12	-
0.06 in Venturi	-		0.18
0.045 in Venturi	-		0.2

The loss coefficients in Table 5.1 can be used to predict losses for the hydrazine system on PACE at a BOL flow rate of 0.1 lbm/s. In this case, the expected pressure loss between the tank and thruster valve inlets would be 10.11 psi if using a 0.060 in venturi, or 30.48 psi if using a 0.045 in venturi.

These predicted values can be compared against the corresponding losses if PACE had flown GHPB by referencing the test data at the same flow rate, for the which the results are tabulated below. Note that since GPHB is denser than hydrazine, an identical mass flow rate of 0.1 lbm/s equates to a volumetric flow rate of just 0.59 GPM. Based on these values, it can be determined that the corresponding pressure losses would be 50.40 psi with a 0.060 in venturi and 109.94 psi with a 0.045 in venturi. This is an appreciable disparity that would result in measurable differences in thrust output, all else being equal. Although this is undesirable, the losses would begin to shrink as mass flow rates decrease over the course of the mission.

Table 5.2: Component Losses at BOL Flow Rate of 0.1 lbm/s

Component	Pressure Loss with N2H4 (psi)	Pressure Loss with GHPB (psi)
Latch Valve	1.70	20.29
Filter	0.45	10.99
0.06 in Venturi	7.96	19.12
0.045 in Venturi	28.33	78.66
PACE Total Loss with a 0.060 in Venturi	10.11	50.40
PACE Total Loss with a 0.045 in Venturi	30.48	109.94

5.2 EOL

Given that PACE is a blowdown system, it is inherently understood that EOL pressure losses will be much less taxing. Although PACE's EOL flow rate is not available, it can be estimated to perform a similar comparison during de-orbit maneuvers. Once again, the *K* values in Table 5.1 are used for the hydrazine system and the test data is used for the GHPB system. An EOL flow rate is estimated to be 0.03 lbm/s, showing the same trend of significantly larger pressure losses when using GHPB. However, at this flow rate, even the GHPB losses are very mild. Note that the latch valve and venturi minimum flow rates are 0.04 lbm/s and 0.06 lbm/s, respectively, so these data points were extrapolated to 0.03 lbm/s.

Table 5.3: Component Losses at the EOL Flow Rate of 0.03 lbm/s

Component	Pressure Loss with N2H4 (psi)	Pressure Loss with GHPB (psi)
Latch Valve	0.15	7.30
Filter	0.04	3.57
0.06 in Venturi	0.72	1.44
0.045 in Venturi	2.55	11.33
PACE Total Loss with a 0.060 in Venturi	0.91	12.31
PACE Total Loss with a 0.045 in Venturi	2.74	22.20

5.3 Design Considerations

To provide a better view of the losses throughout the life of the mission, Figure 5.4 shows the total losses for PACE at various flow rates for a given propellant and venturi size. The data show that losses range from 3-4x larger with GHPB at the maximum flow rate and 8-14x larger at the minimum flow rate. The multiple is larger at the lower flow rates because the total magnitude of the loss with hydrazine is very low at those flow rates. Nonetheless, the disparity between the propellants begins to diminish in consequence at lower flow rates, although it is still appreciable as low as 0.02 lbm/s. Additionally, the data show that losses with GHPB begin to rapidly escalate near PACE's maximum expected flow rate. Even if this prediction is indeed PACE's maximum flow rate, it is unlikely that it bookends the maximum flow rate for a generic low-earth orbit monopropellant satellite.

This could be compensated for by a larger venturi, as it is clear from Figure 5.4 that the selected venturi size will have a significant impact on the total pressure loss. This is true for both propellants, but especially so for GHPB. Referring to the venturi sizes for previous missions that were listed in Table 3.3, the data indicate that GHPB may only be compatible with venturis in the larger half of that range.

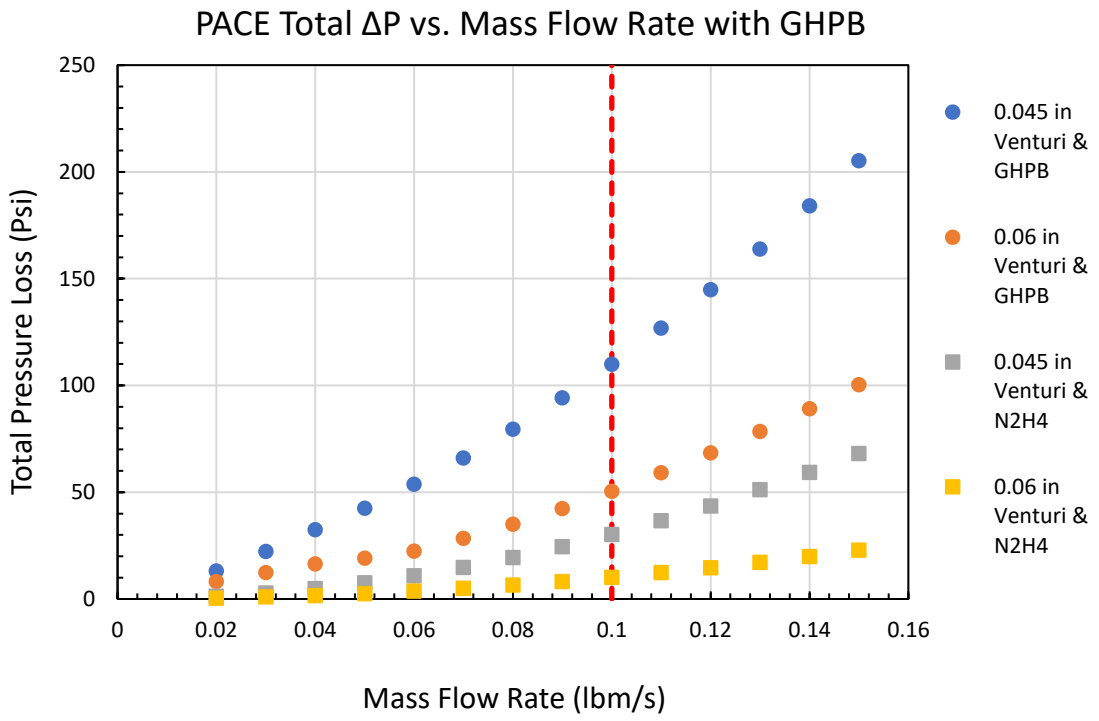

Figure 5.4: PACE's Predicted Total Pressure Loss Based on Venturi Size and Propellant

However, Figure 5.4 does not provide a comprehensive comparison because GHPB is expected to be compatible with larger venturis than hydrazine, all else equal. Recall that venturis are installed to limit the flow rate, and by extension pressure surges, during propulsion system startup. Future testing is planned to confirm this, but the expectation is that the increased viscosity of GHPB will make it less susceptible to damaging pressure surges, which would mean venturis

will not need to be as small to mitigate them. This will be confirmed by tests that quantify pressure spikes under mock flight conditions, but the general trend can be deduced from the Joukowsky equation. This is shown as Equation 5.6, where ΔP_s represents the pressure surge that venturis are typically installed to mitigate, ρ is the density, a is the wave speed, and Δu is the change in fluid velocity upon impact [57].

$$\Delta P_s = -\rho a \Delta u \tag{5.6}$$

Although the wave speed is a function of both the liquid's acoustic velocity and the pipe properties, the pipe properties are constant so it can be represented as the acoustic velocity alone [57]. The acoustic velocities of hydrazine and GHPB at room temperature are similar (2092 m/s and 2065 m/s, respectively [58]), so wave speed is expected to have very little effect on the difference in surge pressure, and the approximation can then be focused on just the changes in density and fluid velocity.

To estimate a change in fluid velocity pre-impact, the latch valve data presented in Figure 4.6 can be used to compare both propellants under otherwise identical flow conditions. Specifically, the respective *K* values with each propellant can be used to modify Bernoulli's equation as shown in Equation 5.7, which reduces to Equation 5.8 when solving for fluid velocity. Doing so indicates that for the same driving pressure, the velocity pre-impact will be approximately four times less for GHPB than it is with hydrazine.

$$P_1 = \frac{1}{2}\rho u_2^2(1+K) \tag{5.7}$$

$$u_2 = \sqrt{\frac{2P_1}{\rho(1+K)}} \tag{5.8}$$

On the other hand, as previously mentioned, GHPB's density is 1.21 times that of hydrazine. Together this indicates the density and fluid velocity will have competing effects on the overall change in surge pressure, but the effect of the decreased velocity due to increased viscosity will be more pronounced than the effect from the increased density.

If the previous analysis is repeated while excluding the venturi from the GHPB system, the total pressure losses can be compared on a more flight-like basis. Since PACE's actual venturi size is 0.052 in (see Table 3.3), this can be used to predict the hydrazine losses. This results in losses with GHPB that are 1.7 – 8.5 times that of hydrazine. However, the higher multiples correspond to lower flow rates where the hydrazine losses are less than 2 psi, and the GHPB losses are likewise mild. Specifically, the losses at the EOL flow rate of 0.03 lbm/s are 1.28 psi and 10.87 psi for hydrazine and GHPB, respectively.

5.4 Mission Impacts

The data show that the burden imposed by GHPB is minimal at the low flow rates typical of an EOL maneuver. It is also likely manageable at BOL flow rates, assuming that GHPB is compatible with larger venturi sizes than hydrazine. If that is not the case, GHPB systems might have too large of a pressure drop to work in a standard blowdown architecture. Consequently, a final determination on whether GHPB can be used in blowdown mode cannot be made until surge testing is completed. This does mean that the advertised capability as a 'drop-in' replacement is yet to be confirmed, although all data indicate that it will be. If losses grow too large for a blowdown architecture, it is not a dealbreaker for the propellant, because pressure-regulated systems are a well-developed technology. The primary drawback is that the system would be

heavier and more complex than a hydrazine blowdown alternative, although some of the weight penalty would be offset by the increased density-I_{sp} of GHPB.

On an actual mission, there are several other variables that affect how consequential the pressure losses associated with GHPB are. For example, the propulsion system layout may contain multiple branches stemming from one tank, meaning the flow rate is divided across the branches. Additionally, certain maneuvers may not need all available thrusters to produce the required ΔV, tanks may have varying pressure and volume ratings, and more. As a result, the effects of the increased pressure losses may range from unacceptable to immaterial across an array of mission profiles, but in general they should be acceptable.

Chapter 6: Conclusion

6.1 Summary

The present study reports pressure losses associated with flows of a novel green propellant known as GHPB through five 'standard' propellant delivery components: a valve, a filter, a fill and drain valve, and two venturis. GHPB is the latest iteration in an industry-wide attempt to replace hydrazine as the standard spacecraft fuel. It retains hydrazine as the base constituent, and it aims to be a hybrid between hydrazine and previous ionic green propellants. The goal is to maintain the low vapor toxicity and high density-I_{sp} of the ionic liquids, while also retaining hydrazine's low flame and preheat temperatures. Retaining hydrazine's low flame temperature allows GHPB to be operated with existing hydrazine hardware, making it a 'drop-in' replacement. This is a key advantage of GHPB over other green propellants.

A novel aspect of these experiments is that they were performed using the 'real' propellant. Safety considerations and the similarity in density and viscosity between hydrazine and water mean that these kinds of tests are normally completed with water as a substitute for hydrazine. However, the additives in GHPB increase the density and viscosity enough that water is no longer a suitable substitute. Therefore, given the frequent use of ionic liquids in green propulsion, and that ionic liquids are generally much more viscous than water, the results of this work extend beyond the scope of GHPB to inform studies of other ionic liquid-based green propellants.

Pressure losses are measured as a function of flow rate in the four types of components. The results are represented using two dimensionless quantities: the loss coefficient K and the discharge coefficient C_d. Limiting pressure drops associated with cavitation are also identified.

These data will be critical knowledge for any mission that proposes to use GHPB, as they are needed to model the thruster injection pressures across a range of operational flow rates. The results show additional losses are incurred with GHPB by comparison to hydrazine in every case, and the extent of the additional losses is dependent on flow rate.

To further investigate the disparity between the propellants, these fundamental component data are used to estimate pressure losses in an actual spacecraft. The spacecraft, named PACE, utilizes a hydrazine blowdown system that is used as a proxy for standard monopropellant architectures. The data show 3-4x larger pressure losses at the maximum flow rate, and 8-14x larger losses at the minimum flow rate. The PACE results also show that GHPB's status as a 'drop-in' replacement may depend on the chosen venturi size. If systems flying GHPB need smaller or equivalently sized venturis by comparison to those used with hydrazine, then the blowdown configuration on PACE would not be possible. Nonetheless, the results suggest that GHPB is likely a 'drop-in' replacement because it is expected to be compatible with larger venturis or none at all. However, complementary tests are needed to confirm this. If PACE were to use GHPB without a venturi, the losses would range from 1.7 – 8.5 times larger than with hydrazine at the maximum and minimum flow rates, respectively.

6.2 Conclusion

The primary conclusion is that as expected, the approximations required to use water as a substitute for testing with hydrazine are no longer valid with this highly viscous propellant. An additional conclusion is that as it pertains to this test, all data suggest that this propellant is indeed suitable for spaceflight. This determination does not encompass all variables that would need to be assessed before a mission, but it can be viewed to include more than just the pressure loss data.

For example, there were no material compatibility concerns, unforeseen safety concerns, or unexpected behaviors during high-pressure flow. There are remaining questions about whether GHPB is compatible with a blowdown architecture, and thus whether it is a true ‘drop-in’ replacement for hydrazine. However, the work presented here contends that it will likely be confirmed to be drop-in replacement.

With respect to the use of this data beyond the scope of GHPB, the conclusion is that it is an important reference point. Clearly the density and viscosity have large effects on the results, so GHPB is not a proxy for other propellants with different material properties. However, given that the majority of flow testing data for these components have been gathered using water or conventional propellants, these results are a valuable addition to data repositories. This will be especially true once surge testing is completed, and a final decision can be made about whether this propellant is prohibitively viscous. This answer will drive design decisions for any future propellant developments with ionic liquids or hybrids.

6.3 Future Work

The highest priority for future work is to conduct surge testing to ensure the propellant is compatible with larger venturis than are used with hydrazine. This is because surge testing and flow testing provide complementary data sets, and they will need to be analyzed together to make a final determination on whether the propellant can be used in blowdown architectures as a drop-in replacement. Although analytical expectations are that GHPB is compatible with blowdown systems, this is particularly crucial to confirm with test data since GHPB is being developed as a monopropellant, and monopropellant systems are usually blowdown. For the purposes of

complementing this data, the surge test analysis should conclude with an anticipated range of venturi sizes that would encompass mission needs.

Additional future work should include finalizing a hazard classification rating for the propellant, which will allow it to be retested without the burden of analog instrumentation. The analog results in this paper are an excellent starting point for evaluation of the propellant in a general sense, but in order to be applied to a specific mission case, a correspondingly specific analysis with more precise instrumentation needs to be completed. When this occurs, future tests should include propellant temperature variations and a thruster valve, both of which require power.

Furthermore, future work could test for the rate of helium and nitrogen saturation into the propellant. This is strongly dependent on tank geometry and was therefore not included in this test, as the propellant tank was not representative of a flight propellant tank. However, pressurant saturation into the propellant will be an important variable to determine since the gas that saturates is generally unrecoverable. This will affect necessary load pressures before launch.

Lastly, since the results here provide an assessment in a broad sense, future work should include testing that is specific to a particular mission. Mission specific variables would include tube lengths, component layouts, flow rates, and given the dependence of the results on viscosity, a range of temperatures representative of the mission profile.

Bibliography

[1] Nufer, B. A Summary of NASA and USAF Hypergolic Propellant Related Spills and Fires. National Aeronautics and Space Administration, 2009, pp. 2-6.

[2] Hazard Communication Standard: Labels and Pictograms. OSHA BRIEF. https://www.osha.gov/sites/default/files/publications/OSHA3636.pdf.

[3] SAFETY DATA SHEET: Hydrazine. Sigma Aldrich. https://www.sigmaaldrich.com/US/en/sds/SIAL/215155.

[4] National Library of Medicine. Hydrazine. https://pubchem.ncbi.nlm.nih.gov/compound/Hydrazine#section=Henry.

[5] Special Project: Fire, Explosion, Compatibility, and Safety Hazards of Hypergols - Hydrazine (AIAA SP-084-1999). 1999, pp 2,132.

[6] Immediately Dangerous to Life and Health Limits. NOAA. https://response.restoration.noaa.gov/oil-and-chemical-spills/chemical-spills/resources/immediately-dangerous-life-health-limits-idlhs.html#:~:text=The%20National%20Institute%20of%20Occupational.

[7] Dear, J. 8-Hour Total Weight Average Permissible Exposure Limit (PEL). | Occupational Safety and Health Administration. www.osha.gov. https://www.osha.gov/laws-regs/standardinterpretations/1995-10-06-3.

[8] Life Support – Propellants. https://public.ksc.nasa.gov/propellants/lifesuppport/.

[9] Chemical - Respirex North America. https://www.respirexna.com/products/chemical

[10] Photostream. Flickr. https://www.flickr.com/photos/nasakennedy/45552839644.

[11] NASA's Green Propellant Infusion Mission Nears Completion. NASA. https://www.nasa.gov/mission_pages/tdm/green/gpim-nears-completion.html.

[12] Sackheim, R., and Masse, R. "Green Propulsion Advancement: Challenging the Maturity of Monopropellant Hydrazine." AIAA JOURNAL OF PROPULSION AND POWER, Vol. 30, No. 2, 2014. https://doi.org/10.2514/1.B35086.

[13] Masse, R. et al., AF-M315E Propulsion System Advances & Improvements.

[14] CHEMICAL MONOPROPELLANT THRUSTER FAMILY. Ariane Group. https://www.space-propulsion.com/brochures/hydrazine-thrusters/hydrazine-thrusters.pdf.

[15] Mohon, L. New Green Propellants Complete Milestones. NASA. https://www.nasa.gov/centers/marshall/news/news/releases/2015/new-green-propellants-complete-milestones.html.

[16] Negri, M. et al., Technology Development for ADN-Based Green Monopropellant Thrusters -an Overview of the Reform Project. Presented at the 7TH EUROPEAN

CONFERENCE FOR AERONAUTICS AND SPACE SCIENCES (EUCASS), 2017DOI: 10.13009/EUCASS2017-319, pp 2-4.

[17] Ravula, S., Larm, N. E., Mottaleb, M. A., Heitz, M. P., AND Baker, G. A., "Vapor Pressure Mapping of Ionic Liquids and Low-Volatility Fluids Using Graded Isothermal Thermogravimetric Analysis." 2019, pp. 42–42. Https://doi.org/10.3390/chemengineering3020042.

[18] Masse, R., Glassy, B., Spores, R., Vuong, A., Zhu, Z., and Pourpoint, T. "Hydrazine-Based Green Monopropellant Blends." AIAA SciTech Forum, 2024. https://doi.org/10.2514/6.2024-1619.

[19] Matter, K. 2020 NASA Announcement of Collaboration Opportunity (ACO) Selections - NASA. NASA. https://www.nasa.gov/missions/station/2020-nasa-announcement-of-collaboration-opportunity-aco-selections/.

[20] McLean, C. et al., "Green Propellant Infusion Mission Program Development and Technology Maturation." American Institute of Aeronautics and Astronautics, pp. 2-13.

[21] RANGE SAFETY USER REQUIREMENTS MANUAL - LAUNCH VEHICLES, PAYLOADS, and GROUND SUPPORT SYSTEMS REQUIREMENTS. SPACE SYSTEMS COMMAND MANUAL, 91-710, VOLUME 3, 2022, p. 11.

[22] Anflo, K., Moore, S., and King, P. Expanding the ADN-Based Monopropellant Thruster Family. 2009. 23rd Annual AIAA/USU Conference on Small Satellites.

[23] Masse, R., Spores, R. A., and Allen, M. "AF-M315E Advanced Green Propulsion – GPIM and Beyond." AIAA Propulsion and Energy 2020 Forum, 2020. https://doi.org/10.2514/6.2020-3517.

[24] AGREEMENT of the MEMBER STATE COMMITTEE on the IDENTIFICATION of HYDRAZINE as a SUBSTANCE of VERY HIGH CONCERN. https://echa.europa.eu/documents/10162/b3561467-aa0f-4551-9dff-dcdc5ba60eec.

[25] Pultarova, T. Hydrazine Ban Could Cost Europe's Space Industry Billions. SpaceNews. https://spacenews.com/hydrazine-ban-could-cost-europes-space-industry-billions/.

[26] Johnson, C. Environmental Life Cycle Criteria for Making Decisions about Green versus Toxic Propellant Selections. Dissertation. The George Washington University, 2012.

[27] Dinardi, A., and Persson, M. High Performance Green Propulsion (HPGP): A Flight-Proven Capability and Cost Game-Changer for Small and Secondary Satellites. 26th Annual AIAA/USU Conference on Small Satellites, p. 10.

[28] Hartman, C., and Bordi, F. "A New Approach to Mission Classification and Risk Management for NASA Space Flight Missions." 2015. https://doi.org/10.13140/RG.2.1.4141.6083.

[29] Mousavi, S. P., Atashrouz, S., Nait Amar, M., Hemmati-Sarapardeh, A., Mohaddespour, A., and Mosavi, A. “Viscosity of Ionic Liquids: Application of the Eyring’s Theory and a Committee Machine Intelligent System.” Molecules, Vol. 26, No. 1, 2020, p. 156. https://doi.org/10.3390/molecules26010156.

[30] Wilcox, D. Basic Fluid Mechanics. D C W Industries, 2012, pp.193-209,310-330.

[31] Flow of Fluids through Valves, Fittings, and Pipe. Crane Co., 1982, pp. 1-1 – 2-15.

[32] Orifice Plates and Orifice Flanges for Flow Measurement. Piping-World. https://www.piping-world.com/orifice-plates-and-orifice-flanges-for-flow-measurement.

[33] Scroggins, A., and Fiebig, M. “Surge Pressure Mitigation in the Global Precipitation Measurement Mission Core Propulsion System.” 50th AIAA/ASME/SAE/ASEE Joint Propulsion Conference, 2014. https://doi.org/10.2514/6.2014-3785.

[34] Special Project: Fire, Explosion, Compatibility, and Safety Hazards of Hypergols - Monomethylhydrazine (AIAA SP-085-1999). 1999, pp 124.

[35] Pure Water Density Standard, UKAS ISO/IEC17025 and ISO Guide 34 Certified, Density: 0.9982 G/ML at 20 C, Density: 0.9970 G/ML at 25 C. *pubchem.ncbi.nlm.nih.gov*. https://pubchem.ncbi.nlm.nih.gov/substance/329798917.

[36] Young, D., Munson, B., Okiishi, T., and Huebsch, W. A Brief Introduction to Fluid Mechanics. John Wiley & Sons, Hoboken, Nj, 2011, pp. 78-89, 275-307.

[37] Miller, D. Internal Flow Systems. The Fluid Engineering Centre, Bedford, UK, 1990, pp. 51-132.

[38] Method-Pressure Drop Tests for Fuel System Components. SAE International, ARP 868D, 2020, p. 5.

[39] White, F. Fluid Mechanics. McGraw Hill, New York, N.Y., 2011, pp. 353-370.

[40] Stinebring, D., Paterson, E., and Straka, W. “Examples of Cavitation and Cavitation Damage.” Penn State Applied Research Laboratory.

[41] Carpenter, J., Badve, M., Rajoriya, S., George, S., Saharan, V. K., and Pandit, A. B. “Hydrodynamic Cavitation: An Emerging Technology for the Intensification of Various Chemical and Physical Processes in a Chemical Process Industry.” Reviews in Chemical Engineering, Vol. 33, No. 5, 2017. https://doi.org/10.1515/revce-2016-0032.

[42] Franc, J.-P. Physics and Control of Cavitation. University of Grenoble, 2006.

[43] Mosier, C. MAP Propulsion System Thermal Design. NASA Goddard Space Flight Center.

[44] Single Line Isolation Latch Valves. Moog. https://www.moog.com/products/propulsion-controls/spacecraft-propulsion/propulsion-components/single-line-isolation-latch-valve.html.

[45] Latch Valves for Missiles and Space. Valcor. https://www.valcor.com/missiles-and-aerospace/aerospace-latch-valves/.

[46] Mikhailovsky, C., Stahl, J., and Mulkey, H. “PACE Propulsion Subsystem Surge Analysis and Testing.” AIAA Propulsion and Energy 2020 Forum, 2020. https://doi.org/10.2514/6.2020-3800.

[47] Flow Venturi Tube. Den Holder. http://www.denholder.com/nwsbrf/denholder-newsletter-march.html.

[48] Fiebig, M., and Zakrzwski, C. “LRO Propulsion System Testing.” 48th AIAA/ASME/SAE/ASEE Joint Propulsion Conference & Exhibit, 2012. https://doi.org/10.2514/6.2012-4331.

[49] Vacco Filtration Catalog. https://www.vacco.com/images/uploads/pdfs/VACCO_Filtration_Catalog_042121_FINAL_with_bookmarks_web.pdf.

[50] Fill and Drain Service Valves. Moog. https://www.moog.com/content/dam/moog/literature/sdg/space/propulsion/moog-manual-fill-and-drain-valves-datasheet.pdf.

[51] Digital Catalog, Dwyer. https://legacy.dwyer-inst.com/catalog/, p. 245.

[52] Test Uncertainty. The American Society of Mechanical Engineers, 2007.

[53] Anderson, W. Rocket Engines. In Encyclopedia of Energy, Vol. 5, Elsevier Inc., 2004, pp. 483–491.

[54] Monopropellant Thrusters. https://www.moog.com/products/propulsion-controls/spacecraft-propulsion/thrusters/monopropellant-thrusters.html.

[55] Diaphragm Tanks Data Sheets – Sorted by Volume. Northrop Grumman. https://www.northropgrumman.com/space/diaphragm-tanks-data-sheets-sorted-by-volume.

[56] Low Pressure Latch Valves. Vacco. https://www.vacco.com/images/uploads/pdfs/latch_valves_low_pressure.pdf.

[57] Walters, T. W., and Leishear, R. A. “When the Joukowsky Equation Does Not Predict Maximum Water Hammer Pressures.” Journal of Pressure Vessel Technology, Vol. 141, No. 6, 2019. https://doi.org/10.1115/1.4044603.

[58] DeSain, J., and Brady, B. Thermal Conductivity and Speed of Sound Measurements of Liquid Hydrazine (N2H4) at 293.15K and 0.101 MPa to 2.068 MPa. Space Materials & Physical Sciences Laboratory, The Aerospace Corporation, 2008, p. 2.